Penalized Maximum Likelihood Based Localization for Unknown Number of Targets Using WSNs: Terrestrial and Underwater Environments

Mohammad Al-Jarrah, *Member, IEEE,* Emad Alsusa, *Senior Member, IEEE*, and Arafat Al-Dweik, *Senior Member, IEEE*

***Abstract*—This paper proposes a multiple target localization scheme using a clustered wireless sensor network (WSN) for terrestrial and underwater environments. In the considered system, sensors measure the total energy emitted by the targets and transmit quantized versions of their measurements to a data central device (DCD) with the help of intermediate cluster-heads (CHDs), which employ decode-and-forward relaying (DFR). Upon data collection from sensors, the DCD performs the localization process, which involves estimating the number and positions of the targets. Data transmission from the sensors to CHDs takes place through an imperfect medium, which is characterized by a Rician fading model. The penalized maximum likelihood estimator (PMLE), also known as regularized maximum likelihood estimation (MLE), is applied at the DCD to provide optimal estimates of the number and locations of targets. Furthermore, a suboptimal estimator is derived from PMLE that offers comparable performance under certain operating conditions, but with significantly reduced computational complexity. Cramer-Rao lower bound (CRLB) is derived to serve as an asymptotic benchmark for the root mean square error (RMSE) of the estimators in addition to the centroid-based localization benchmark. Monte Carlo simulation is used to evaluate the performance of the proposed estimation techniques under various system conditions. The results show that PMLE can effectively estimate the number and locations of the targets. Furthermore, it is shown that the RMSE of the proposed estimators approaches the CRLB for a large number of sensors and a high signal-to-noise ratio.**

***Index Terms*—Target localization, penalized maximum likelihood, Bayesian information criterion (BIC), Hannan-Quinn information criterion, Akike information criterion, M-ASK modulation, WSN, underwater localization.**

List of Acronyms

ACD amplitude coherent detection.
AIC Akike information criterion.
AoA angle-of-arrival.
AUV autonomous underwater vehicles.
AWGN additive white Gaussian noise.
BIC Bayesian information criterion.
cAIC corrected Akike information criterion (AIC).
CD coherent detection.
CDF cumulative distribution function.
CHD cluster-head.
cMLD coherent maximum likelihood detector.
CRLB Cramer-Rao lower bound.
CSI channel state information.
DCD data central device.
DFR decode-and-forward relaying.
DTE decode-then-estimate.
ECC equalization-clustering-centroid.
ED energy detector.
EM electromagnetic.
FDMA frequency division multiple access.
FIM Fisher information matrix.
GA Genetic algorithm.
HQIC Hannin-Quinn Information Criterion.
IoT Internet of things.
LoS line-of-sight.
LSE least square estimation.
ML maximum likelihood.
MLE maximum likelihood estimation.
NCED noncoherent energy detection.
PDF probability density function.
PMLE penalized maximum likelihood estimator.
PSER pairwise symbol error rate (SER).
RF radio frequency.
RMSE root mean square error.
RoI region of interest.
RSS received signal strength.
SCDP symbol correct detection probability.
SER symbol error rate.
SNR signal-to-noise ratio.
TDMA time-division-multiple-access.
TDoA time-difference-of-arrival.
ToA time-of-arrival.
UAV unmanned aerial vehicles.
UW underwater.
WSN wireless sensor network.

M. A. Al-Jarrah and E. Alsusa are with the School of Electrical and Electronic Engineering, University of Manchester, Manchester M13 9PL, UK (e-mail: {mohammad.al-jarrah, e.alsusa}@manchester.ac.uk).

A. Al-Dweik is with 6G Research Center, Department of Computer and Communications Engineering, Khalifa University, Abu Dhabi, P.O.Box 127788, UAE. (e-mail: arafat.dweik@ku.ac.ae). He is also with the Department of Electrical and Computer Engineering, Western University, London, ON, Canada. (e-mail: dweik@fulbrightmail.org).

I. Introduction

Wireless sensor networks (WSNs) play a key role in the emerging Internet of things (IoT) paradigm. WSNs are typically designed to sense the surroundings and feed the sensed data to the Internet cloud for data analysis, real-time monitoring, decision-making, etc. [1], [2]. WSNs have several key features that make them well-suited for various applications in different sectors. Such features include: 1) Cost

effectiveness as WSN typically consists of a large number of small and inexpensive sensing nodes that are deployed in large quantities, 2) Low power consumption as the sensors are typically designed to operate using a limited power battery or using energy harvesting modules, allowing them to operate for extended periods without requiring frequent battery replacement or recharging, 3) Flexibility because sensors can be easily deployed and reconfigured to adapt to environmental conditions, which enables scalability and reconfigurability without significant disruption, 4) Mobility where the network topology can support mobile nodes, enabling applications that involve tracking or monitoring of objects or individuals in motion, e.g., intelligent transportation systems, 5) Extended coverage area, which can be achieved by cooperatively relaying data among several nodes, and 6) Small size where sensing nodes are typically compact and unobtrusive, allowing them to be deployed in various locations without attracting attention or interfering with the surrounding environment. Due to these features, WSNs have applications in various sectors, including military operations, industrial monitoring and control, health care and medical systems, intelligent transportation systems, smart cities, environmental monitoring, etc. [1]–[3].

The problem of target detection and localization is one of the most popular applications of WSNs [4]–[9]. While target detection focuses on identifying the presence of a target, localization goes a step further by estimating the spatial position. This additional information is crucial for many practical scenarios in which knowing the location of targets is crucial for effective actions and decision-making. Fig. 1 shows an illustrative diagram of a clustered terrestrial WSN deployed to localize unmanned aerial vehicless (UAVs), where each cluster-head (CHD) sends its data to data central device (DCD) through a cellular network. Localization using WSNs has gained significant attention from researchers, where various algorithms have been proposed to address this problem. These algorithms typically involve the collaboration and coordination of spatially distributed sensors within the network [10]–[14]. A general overview of the localization process can be summarized as follows [15]–[25]:

1) Data collection process, in which sensors collect measurements from the targets of interest. This can be done individually or cooperatively, where sensors collaborate to gather more comprehensive information.
2) Local processing, where each sensing node processes its collected data and extracts relevant features or measurements/observations related to the targets. Local processing may involve various signal processing schemes, such as noise filtering, quantization, or feature extraction techniques for sophisticated or intelligent sensors.
3) Transmission of the decision or quantized measurements to DCD. It should be noted that transmitted decisions usually include the processed data and any other relevant metadata, and transmissions may take place through intermediate devices called CHDs.
4) Estimation of the locations of the targets at the DCD, which uses data collected from sensors to estimate the number and spatial coordinates of the targets. The estimation process can be performed using techniques such as trilateration, multilateration, triangulation, etc. By leveraging the information collected from multiple sensors, the DCD can achieve a more reliable target localization. Location information is beneficial for various applications, such as location-based services, autonomous vehicles, rescue missions, environment monitoring, navigation in challenging environments, and defense surveillance missions. It is worth noting that different localization algorithms may have different accuracy and system design requirements, such as network topology and computational resources. Adopting a particular algorithm depends on the specific application, the desired accuracy, and the constraints of the WSN deployment.

Sensors may employ various measuring techniques to contribute to the localization process at the network level. These techniques include angle-of-arrival (AoA), time-of-arrival (ToA), time-difference-of-arrival (TDoA), and received signal strength (RSS) [14]–[23]. In AoA based localization, the sensors use antenna arrays to determine the angle of the incident signal. However, this approach introduces additional overhead in terms of size and cost of the sensing nodes due to the requirement of antenna arrays [18], [19]. On the other hand, ToA-based and TDoA-based systems rely on accurate time synchronization between the sensors. By measuring the time it takes for the signals to propagate from the source to the sensors, the distance between the sensors and the source can be estimated [20], [22], [23]. However, to achieve accurate localization, precise time synchronization is essential, which requires considerable complexity. However, RSS-based localization is considered simple and cost-effective compared to the aforementioned AoA, ToA and TDoA techniques. In RSS-based localization, the sensors measure the power level of the received signal, which is influenced by factors such as distance, obstacles, and interference. By analyzing the RSS values collected by multiple sensors, the network can extract useful information about the target location. Although RSS-based localization may not achieve the accuracy of other techniques, it has attracted significant interest due to its low complexity [14], [16], [17], [22], [23]. Moreover, localization accuracy can be further enhanced by deploying multiple low-cost, spatially distributed sensors. However, the selection of a measuring technique depends on the trade-offs between the required accuracy, computational and hardware complexities, and cost-effectiveness. Ongoing research continues to explore and develop measuring methods to achieve higher degrees of accuracy and improve the applicability of WSN-based localization.

A. Related Literature

Due to its powerful computational capacity, the DCD can generally handle complex computations that could be required to improve the overall localization accuracy. In the literature, several approaches have considered a DCD to achieve the targets' localization objective. For example, a localization scheme is proposed in [10] for mobile WSNs based on discrete

This article has been accepted for publication in IEEE Internet of Things Journal. This is the author's version which has not been fully edited and content may change prior to final publication. Citation information: DOI 10.1109/JIOT.2023.3347171

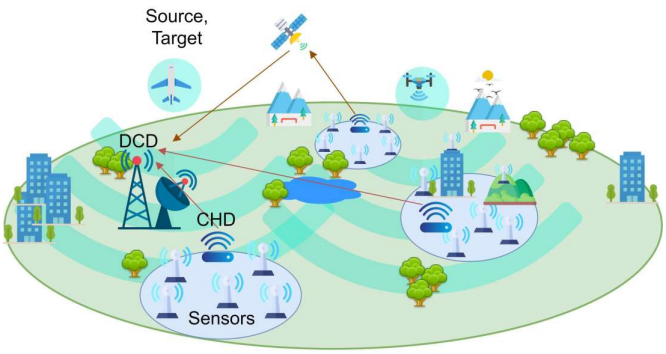

Fig. 1. Typical structure for terrestrial WSN deployed to localize UAVs.

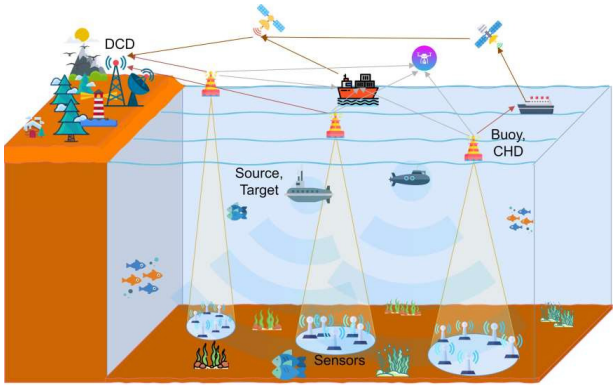

Fig. 2. Network structure of UW-WSN deployed to localize AUVs.

measurements for the energy intensity field produced by the target. A maximum likelihood estimation (MLE) with quantized decisions sent over Rayleigh fading channel is proposed in [14]. Error control coding is applied in [11], as well as error concealment algorithms at the DCD are proposed in [16] and [17] based on majority voting and connected graph algorithms, respectively, to correct the measurements received based on their spatial distribution. Hybrid RSS/AoA observations are considered in [18] and [19], where semi-definite programming and convex relaxation are applied to fuse the measurements.

In [26], a bit allocation algorithm is introduced for rate-constrained localization to quantize the RSS measurements while satisfying error requirements in a squared error sense. The impact of the transmission power uncertainty on RSS-based localization is considered in [27], where a two-phase optimization method is proposed to satisfy non-negative constrained least squares. The first phase of the proposed algorithm is based on a matrix factorization approach, while the second phase employs a max-min strategy based on Taylor linearization. Furthermore, a range-based localization approach is proposed in [28], where sensors are used to measure the distance to a target. In addition, localization using unlabeled data sent from the sensors to the DCD is considered in [29] by exploiting the underlying geometrical structure of the inference problem using partitioning and intersection-based methods. Indoor localization algorithm using distributed set-membership filtering based RSS measurements is proposed in [30] under bounded unknown noise, and a similar filtering method is employed in [31] for target tracking. Cubature Kalman filter is used in [32] for RSS-based mobile target tracking in resource-constrained WSN under RSS quantization uncertainties.

Along the same lines, underwater target localization using sensor networks is focuses on accurately determining the positions of targets or objects in underwater environments. This information is crucial for a wide range of applications such as underwater surveillance, environmental monitoring, marine exploration, scientific investigation, and underwater robotics. The main challenges of underwater localization include limited visibility, harsh acoustic conditions, and signal propagation characteristics. Among the various technologies developed for underwater communication including acoustic, optical, and hybrid approaches, acoustic signaling is still the dominant technology, because the optical approach requires clear water conditions [33], [34]. It should be noted that acoustic-based localization methods are widely used in underwater environments because of the excellent propagation characteristics of sound waves in such a medium. Fig. 2 shows an example for underwater (UW)-WSN used to localize autonomous underwater vehicless (AUVs) where a number of surface buoys are deployed to operate as CHDs. The underwater localization methods are not drastically different from their terrestrial counterparts. For example, in [12], optimal placement of sensors is considered for underwater sensors by maximizing the determinant of the Fisher information matrix (FIM) using range measurements. Efficient and accurate localization schemes are proposed in [35] based on distance-based and AoA measurements. Furthermore, a novel localization scheme is developed in [36] for UW-WSN, named communication signal propagation loss localization, which is based on propagation loss. In [37], an iterative localization is developed based on mobile self-sinking beacon technology, which suits large scale UW-WSNs. The impact of imperfections, such as sea current fluctuations, is addressed in [38] and [39]. Furthermore, a semi-blind passive localization algorithm is developed in [40] with the aim of estimating the source's position for scenarios in which the line-of-sight (LoS) between the source and a subset of sensors might be abscent. Moreover, the authors in [41] have established a testbed for scuba diver navigation assisted by AUV and introduced location estimation algorithms and a communication architecture. Table I summarizes the distinctive characteristics of the literature surveyed in this subsection, where S/M denotes the assumption made on the number of targets, i.e., single/multiple targets deployed.

B. Motivation and Contribution

Although the aforementioned studies contribute to the development of accurate and efficient localization solutions for WSNs, the problem of multiple target localization with unknown quantity has not been comprehensively addressed under non-ideal quantization and imperfect signal transmission. For example, the work in [43]–[46] assumed that the number of targets is priorly known, whereas the work in [47], [48] neither considers the non-ideal quantization performed by the sensors nor the channel imperfections. Consequently, this paper

TABLE I
A SUMMARY FOR THE RELATED LITERATURE IN SEC. I-A.

Reference	UW-WSN/ T-WSN	S/M	L	Fading	Quantization	Clustered WSN	Measurements	Localization algorithm
[10]	T-WSN	M	known	✗	✓	✗	RSS	partial Delaunay triangulation
[11], [14], [16]		S	N/A	✓	✓	✗	RSS	MLE
[17]		S	N/A	✓	✓	✗	RSS	linear regression
[18], [19]		S	N/A	✗	✗	✗	RSS/AoA	least square estimation (LSE)
[26]		S	N/A	✗	✓	✗	RSS	MMSE
[27]		S	N/A	✗	✗	✗	RSS	LSE/matrix factorization
[28]		S	N/A	✗	✗	✗	range/ToA	distance matrix factorization
[29]		S	N/A	✗	✗	✗	range	multilateration
[30]		S	N/A	✗	✗	✗	RSS	set-membership filtering
[31]		M	known	✗	✗	✗	RSS	adaptive set-membership filtering
[32]		M	known	✗	✓	✗	RSS	adaptive Kalman filter
[12]	UW-WSN	S	N/A	✗	✗	✗	range	MLE
[35]		S	N/A	✗	✗	✗	range/AoA	Kalman Filter
[36]		S	N/A	✗	✗	✗	RSS	multilateration/Centriod
[37]		M	known	✗	✗	✓	range	LSE
[38]		M	known	✗	✗	✓	frequency analysis	deep information-based weight fusion
[39]		S	N/A	✗	✗	✓	range/AoA	triangularization/particle system based
[40]		S	N/A	✓	✓	✗	RSS	MLE
[41]		S	N/A	✗	✗	✗	range	factor graph inference

considers wireless channel-aware localization using WSNs for unknown number of targets. The system model consists of a clustered WSN, where the sensors in each cluster send their quantized measurements to the associated CHD using M-ary amplitude shift keying (M-ASK), after which the CHDs relay the measurements to the DCD, which is responsible for estimating the number and locations of targets. To capture the system imperfections, non-ideal RSS measurements at the sensors are considered, and transmissions between the sensors and CHDs, and between the CHDs and DCD, are subject to Rician fading. In addition, a generalized sensing model is adopted to characterize two stimulating localization environments, namely, underwater acoustic propagation and terrestrial propagation models, and the impact of the quantization process at the sensors is taken into account. To achieve this objective, the penalized maximum likelihood estimator (PMLE) is applied at the DCD, where a penalty term that depends on the number of targets, is used to penalize the maximum likelihood (ML) function. The main contributions of this work can be summarized as:

1) The development of the optimal estimation approach based on PMLE for estimating the number and locations of targets. Several penalization methods are considered and compared, including Bayesian information criterion (BIC), also known as the Schwarz criterion, Akike information criterion (AIC), corrected AIC (AIC), and Hannin-Quinn Information Criterion (HQIC), where the penalty term depends on the number of estimated parameters, and thus it is utilized to estimate the number of targets.
2) An analytical suboptimal localization algorithm is derived from PMLE, which enables the trade-off between complexity and performance. The suboptimal algorithm is based on the high signal-to-noise ratio (SNR) approximation, and provides asymptotically near-optimal performance.
3) A lower bound for the root mean square error (RMSE) of the proposed estimator is derived using the Cramer-Rao lower bound (CRLB) theorem based on FIM.
4) A simple design method is introduced for the thresholds that are used by the sensors to quantize their RSS measurements.
5) The system design and analysis are carried out using three types of detection at the receiving ends of communicating devices. More specifically, coherent detection (CD) in which the receiver requires complete channel state information (CSI), amplitude coherent detection (ACD) that requires the instantaneous channel envelope only, and noncoherent energy detection (NCED) that does not need any kind of information about the instantaneous characteristics of the channel. Moreover, approximations for symbol error rate (SER) of M-ASK signalling with CD and NCED reception are derived under Rician fading channel to provide simple and traceable SER formulae, which to the best of the authors' knowledge have not been derived before.
6) The results obtained reveal that the proposed PMLE is a powerful tool to estimate the number and locations of targets, and the RMSE of PMLE converges to the derived CRLB when SNR and number of sensors are sufficiently large.

The remainder of the paper is organized as follows. In Sec. II, the system model and network topology are introduced. The processing of collected measurements at the sensors is explained in Sec. III, while Sect. IV investigates the detection and relaying methods at the CHDs. The location estimation process at the DCD is developed in Sec. V, and estimating the number of targets using the PMLE is discussed in Sec. VI. The derivations of the CRLB are carried out in Sec. VII. Sec. VIII presents the simulation results, and finally, the paper is concluded in Sec. IX.

II. System Model

This work considers a large-scale WSN consisting of K sensors distributed in a region of interest (RoI) with known positions to collect and quantize observations originated by L active targets, termed as emitters or sources. The sensors considered are low-cost and have limited computational capacity, that is, they can only measure and quantize the RSS. The sensors cannot distinguish the signals of different emitters and thus measure the total power received from all existing emitters. In addition, sensory measurements are quantized using a set of pre-designed thresholds, and modulated using M-ary amplitude shift keying (M-ASK). Unipolar M-ASK transceivers are attractive for WSNs applications due to their simple design, the possibility of applying noncoherent and ACD, and are energy efficient, since sensors with 0 decisions remain silent to save energy.

A. Network Topology

Fig. 3 shows a block diagram that illustrates the considered network topology by revealing the relationship between different nodes in the network. The sensors are divided into C clusters, each of which is supported by a CHD to which the sensors send their decisions. The CHDs apply decode-and-forward relaying (DFR) to send decisions to the DCD, which is responsible for the estimation process. The sensors clustering can save transmission energy, increase the longevity of the network by avoiding long-distance transmission. In addition, we consider a generalized sensing model that is applicable for terrestrial WSN (T-WSN) and UW-WSN, and aims to localize a number of electromagnetic (EM) sources and acoustic wave sources (emitters), respectively. The number of sensors per cluster is denoted by $K_i, i \in \{1, 2, \ldots, C\}$, and without loss of generality, each cluster is assumed having $K_i = \dfrac{K}{C} \triangleq K_{\mathrm{c}}$ sensors. The emitters' signals are also subject to LoS conditions. A detailed description of the signaling type, sensing link, and communication links between each pair of devices in the network is summarized in Table II for the T-WSN and UW-WSN.

B. Rician Fading Model

The sensors-CHDs and CHDs-DCD links are modeled using the Rician distribution in which the received signal has a LoS component in addition to multipath reflections, which randomly affect the envelope and phase of the received signal. The Rician factor $\mathcal{K}$ specifies the link quality, for example the case when $\mathcal{K} \to \infty$ indicates that the link has no fading. It is worth mentioning that for underwater acoustic signal transmission from sensors to their associated CHDs, which is actually a buoy, Rician model is selected as a practical model because it captures the received fluctuations caused by the wobbly buoy due to water surface waves, as well as, to model reflections of acoustic signals from the water surface and sea bottom [49], [50]. The Rician channel coefficient $h \sim \mathcal{CN}\left(m_h, 2\sigma_h^2\right)$, where the joint and marginal probability density functions (PDFs) of the channel envelope $\alpha \triangleq |h|$ and phase $\phi \triangleq \arg\{h\}$ can be found in [51]. It is noteworthy

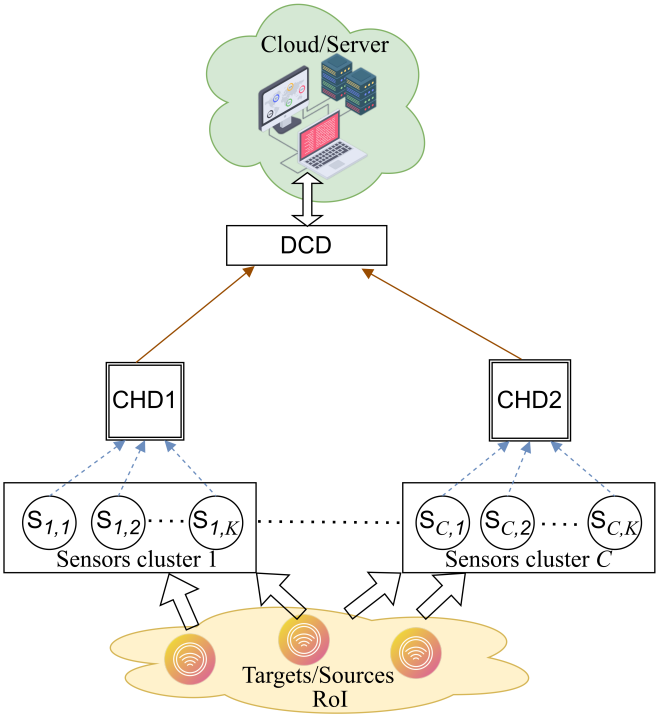

Fig. 3. A block diagram illustrating the network topology.

mentioning that the Rician channel can be also characterized using $\Omega \triangleq \mathrm{E}\left[\alpha^2\right] = \mu_h^2 + 2\sigma_h^2$ with $\mu_h = |m_h|$ and $\mathcal{K} = \frac{\mu_h^2}{2\sigma_h^2}$, $\mathcal{K} \in [0, \infty)$. For small values of $\mathcal{K}$, the channel fading becomes severe, which indicates a poor link quality, while high quality links are typically achieved when $\mathcal{K} \gtrsim 10$. The PDF of ϕ can be approximated as a von Mises distribution, also known as the Tikhonov or circular Gaussian distribution, which is typically characterized by μ_{v} and $\kappa_{\mathrm{v}} \triangleq \sqrt{2\mathcal{K}\left(\mathcal{K}+1\right)}$ which represent the mean and shape parameters, respectively. The uniform phase distribution, which occurs when the environment is extremely reflective, is a special case of the von Mises model and can be obtained by setting $\kappa_{\mathrm{v}} \to 0$. Moreover, with the von Mises model, the random variation in the phase of the received signal, which is produced due to reflections of radio frequency (RF) or acoustic signal from surrounding objects, water surface, sea bottom, etc., can be perfectly captured. For example, for small values of κ_{v}, the non-LoS (nLoS) reflected components dominate the received signal, while the LoS component starts dominating the received signal as κ_{v} increases.

C. Estimators Design and Analysis Overview

As the main objective of this work is to estimate the number and locations of the targets using the network topology described in Fig. 3, the signal processing methods carried out at the sensors, relays, and DCD should be investigated and their achievable performance needs to be evaluated. Therefore, Sec. III is dedicated to investigating the energy detection and signal processing algorithms applied by sensors, as well as the sensory decision statistics, which will be used not only

TABLE II
A SUMMARY FOR THE COMMUNICATION LINKS OF THE IOT NETWORK.

	Terrestrial WSN (T-WSN)		UW-WSN	
Link Endpoints	Signaling	Channel Model	Signaling	Channel Model
Target-Sensor	EM waves	LoS, additive white Gaussian noise (AWGN)	Acoustic	LoS, AWGN
Sensor-CHD	EM waves, MASK	Rician fading, AWGN	Acoustic	Rician fading, AWGN
CHD-DCD	EM waves, MASK	Rician fading, AWGN	EM waves, MASK	Rician fading, AWGN

to characterize the sensing performance, but also to design the estimation methods. In addition, a review of the DFR is introduced in Sec. IV where CD, ACD and NCED are provided, and expressions for the pairwise error and correct probabilities are derived to be used for the design of the optimal coherent MLE. Thereafter, in Sec. V, the mathematical derivations for three novel kinds of estimators, i.e., CD-based, ACD-based and NCED-based estimators, are performed to provide a trade-off between the computational complexity and localization accuracy. In addition, a novel estimation method, denoted as decode-then-estimate (DTE), is derived to provide a low complexity estimator at the expense of achievable RMSE, which is expected to converge to the optimal estimator when SNR is large. Then, the development of the estimators to adapt for the case of unknown number of targets is presented in Sec. VI using several information criteria. Finally, the mathematical derivations for CRLB, which is a typical bound that measures the efficiency of estimators, are provided in Sec. VII.

III. PROCESSING AT SENSING NODES

For an emitter-sensor channel with LoS propagation medium, the EM/acoustic signals will be subject to large-scale pathloss. Accordingly, the decay of the emitter signal typically depends on the signaling type, distance between emitters and sensors, and propagation medium. For example, an acoustic signal decay factor in an underwater environment is generally different from RF signal propagating in space/air. Therefore, the received power, which is sent by a target (emitter or source) l, and received at the kth sensor can be generally expressed as [49], [54], [55]

$$B_k^l\left(d_k^l, f\right) = P_l\left(\frac{d_0}{d_k^l}\right)^{\kappa} a\left(f\right)^{\left(d_0 - d_k^l\right)^{\varrho}}. \tag{1}$$

Here;

- d_k^l is the distance between the emitter l and sensor k, and d_0 is a reference distance that is typically set to 1 m. Given the vector of unknown targets locations in Cartesian coordinates, $\boldsymbol{\theta} = [x_1, y_1, z_1, x_2, y_2, z_2, \cdots, x_L, y_L, z_L] \in \mathbb{C}^{1\times 3L}$, the actual distance between sensor k and target l, i.e., d_k^l, can be written as $d_k^l = \sqrt{\left(x_k - x_l\right)^2 + \left(y_k - y_l\right)^2 + \left(z_k - z_l\right)^2}$ where (x_l, y_l, z_l) and (x_k, y_k, z_k) are the Cartesian coordinates of the lth target and kth sensor, respectively.
- κ is defined as the spreading factor of the underwater acoustic medium for which κ describes the geometry of propagation with typical values ranging from 1 to 2, while for the free space RF it is the pathloss exponent with values ranging from 2 to 4.
- $a\left(f\right)$ is the absorption coefficient which is given by Thorp's formula $10\log a\left(f\right) = \frac{0.11f^2}{1+f^2} + \frac{44f^2}{4100+f^2} + 2.75\times 10^{-4}f^2 + 0.003$ dB/km for underwater acoustic signals propagation with f in kHz, whereas for RF signals it is calculated using Friis formula at the reference distance d_0, i.e., $a\left(f\right) = G_T G_R\left(\frac{c}{4\pi f d_0}\right)$ with $c = 3\times 10^8$ m/s and f are respectively the speed of light and the signal frequency. Without loss of generality, we assume that the antenna gains are normalized to unity, i.e., $G_T = G_R = 1$.
- $\varrho \in \{0, 1\}$ for RF and underwater transmission mediums, respectively. It is noteworthy mentioning that the decaying in the transmit power for the RF signal due to frequency f, i.e., the term $a\left(f\right)^{\left(d_0 - d_k^l\right)^{\varrho}}$, is independent of the distance d_k^l (e.g. $\left(d_0 - d_k^l\right)^{\varrho} = 1$ since $\varrho = 0$), whereas it is dependent on d_k^l for underwater scenarios (e. g. $\varrho = 1$).

Although the value of P_l might not be known in some applications, there is a wide range of applications in which it is known in advance such as cooperative target localization, anchor node localization, or any other application in which targets are not malicious intruders [2], [11], [13]. Therefore, since the focus is on estimating the number and locations of targets, P_l is assumed to be known at the DCD. Moreover, to efficiently use the limited network resources, each sensor handles a number of T observations (or snapshots) to obtain a reliable decision that is sent to the CHD using orthogonal channels such as time-division-multiple-access (TDMA) and/or frequency division multiple access (FDMA), where targets are assumed to be stationary during the period of consecutive T snapshots. This approach can reduce the communication overheads including bandwidth, time, and energy consumption compared to the scenario in which each sensor generates and sends a decision based on a single observation. Moreover, the observations pass through a low complex energy detector (ED), thus the decision statistic is a sum of T energy readings. Consequently, using the superposition principle, the observed signal at the kth local sensor during the tth observation period, $\tilde{s}_k[t]$, which depends on the total power received from all targets, can be written as

$$\tilde{s}_k[t] = \left|\sum_{l=1}^{L} A_k^l\left(\boldsymbol{\theta}\right) + w_k[t]\right|^2 \tag{2}$$

where $A_k^l\left(\boldsymbol{\theta}\right) \triangleq \sqrt{B_k^l\left(\boldsymbol{\theta}, f\right)}$ with $\boldsymbol{\theta}_l = [x_l, y_l, z_l] \in \mathbb{C}^{1\times 3}$ is the Cartesian coordinates of target l, and $w_k[t] \sim \mathcal{N}\left(0, \sigma_w^2\right)$ is the AWGN. Consequently, the average of T observations can be represented as

$$s_k \triangleq \frac{1}{T}\sum_{t=1}^{T}\tilde{s}_k[t] = \sum_{t=1}^{T}\left|\sum_{l=1}^{L}\frac{A_k^l\left(\boldsymbol{\theta}\right)}{\sqrt{T}} + \frac{w_k[t]}{\sqrt{T}}\right|^2, \tag{3}$$

and thus, the quantization carried out by sensors can be represented as

$$d_k = \begin{cases} 0, & \tau_{-1} < s_k < \tau_0 \\ 1, & \tau_0 \leq s_k < \tau_1 \\ \vdots & \vdots \\ M-1 & \tau_{M-2} \leq s_k < \tau_{M-1} \end{cases}, \quad (4)$$

where M is the number of quantization levels which is equal to the modulation order, and thresholds $\{\tau_{-1}, \tau_{M-1}\} = \{0, \infty\}$.

A. Quantized Decision Statistics

It can be noticed that the distribution of $A_k^{\Sigma}(\boldsymbol{\theta}) + w_k[t]$ with $A_k^{\Sigma}(\boldsymbol{\theta}) = \sum_{l=1}^{L} A_k^l(\boldsymbol{\theta})$ conditioned on $A_k^{\Sigma}(\boldsymbol{\theta})$ follows normal distribution with a mean of $A_k^{\Sigma}(\boldsymbol{\theta})$ and a variance of σ_w^2, i.e., $\mathcal{N}\left(A_k^{\Sigma}(\boldsymbol{\theta}), \sigma_w^2\right)$. Therefore, by noting that $\frac{A_k^{\Sigma}(\boldsymbol{\theta})}{\sqrt{T}} + \frac{w_k[t]}{\sqrt{T}} \sim \mathcal{N}\left(\frac{A_k^{\Sigma}}{\sqrt{T}}, \frac{\sigma_w^2}{T}\right)$, it can be concluded that s_k is noncentral Chi-squared distributed with T degrees of freedom and noncentrality parameter of $\check{s} = A_k^{\Sigma}(\boldsymbol{\theta})$, whose PDF and cumulative distribution function (CDF) are respectively given by [56]

$$f_{s_k}(x) = \frac{T}{2\sigma_w^2}\left(\frac{x}{\check{s}^2}\right)^{\frac{T-2}{4}} \mathrm{e}^{-T\left(\frac{x+\check{s}^2}{2\sigma_w^2}\right)} I_{T/2-1}\left(\frac{T\check{s}}{\sigma_w^2}\sqrt{x}\right), \quad (5)$$

and

$$F_{s_k}(x) = 1 - Q_{T/2}\left(\sqrt{T}\frac{\check{s}}{\sigma_w}, \sqrt{T}\frac{\sqrt{x}}{\sigma_w}\right) \quad (6)$$

where $I_q(\cdot)$ is the modified Bessel function of the first kind and order q, and $Q_q(\cdot,\cdot)$ is the generalized marcum Q-function of order q. However, for more accurate results, T is typically large and thus the distribution of s_k can be approximated as Gaussian PDF using Central Limit Theorem (CLT), i.e., $s_k \sim \mathcal{N}\left(\mu_{s_k}(\boldsymbol{\theta}), \sigma_{s_k}^2(\boldsymbol{\theta})\right)$ with $\mu_{s_k}(\boldsymbol{\theta}) = \sigma_w^2 + \left(A_k^{\Sigma}(\boldsymbol{\theta})\right)^2$ and $\sigma_{s_k}^2(\boldsymbol{\theta}) = \frac{2\sigma_w^4}{T} + 4\frac{\sigma_w^2}{T}\left(A_k^{\Sigma}(\boldsymbol{\theta})\right)^2$. Based on CLT approximation, and with the aid of (3) and (4), the decision statistics can be easily derived as

$$\Pr(d_k = m|\boldsymbol{\theta}) = Q\left(\frac{\tau_{m-1} - \mu_{s_k}(\boldsymbol{\theta})}{\sigma_{s_k}(\boldsymbol{\theta})}\right) - Q\left(\frac{\tau_m - \mu_{s_k}(\boldsymbol{\theta})}{\sigma_{s_k}(\boldsymbol{\theta})}\right) \quad (7)$$

where $m \in \{0, 1, \ldots, M-1\}$ and $Q(\cdot)$ is the complementary CDF of a normal random variable.

The final task of sensors is to modulate their decisions using unipolar M-ASK before transmitting them to the corresponding CHDs. For unipolar M-ASK modulation with uniform amplitude spacing, i.e., $s_{m+1} - s_m = \delta \ \forall\ m = \{0, 1, \ldots, M-1\}$, and normalized energy, i.e., $\sum_{m=0}^{M-1} s_m^2 = 1$, the baseband representation of the transmitted signal from sensor k is given by [51]

$$u_k^{(m)} = m \times \delta, \quad \delta = \sqrt{\frac{6}{(2M-1)(M-1)}}. \quad (8)$$

The modulation order M is basically equal to the number of quantization levels.

B. Quantization Thresholds Design

The design of thresholds $\tau_{m-1}\ \forall m \in \{0, 1, \ldots, M\}$ in (4) should take into account that for a certain target, the far-away detectors should have decisions 0, which guarantee power savings. On the other hand, close-by detectors should have decisions of $M-1$, and the ones with a distance between these two extreme cases take values from 1 to $M-2$ with the closer detector having a higher quantization level. Therefore, if we assume that highly densified WSN is deployed uniformly over a two-dimensional (2D) circular area of diameter R m, the received signal is noiseless, and the target is located in the middle of that circle (i.e., the furthest sensor is $0.5R$ m away from the target), then roughly speaking, the network can be divided into a number of M tiers each of which is $\frac{R}{2M}$ m wide. Subsequently, the threshold can be calculated with the aid of (1) as

$$\tau_{M-m-2}(\boldsymbol{\theta}) = P_l\left(\frac{1}{(m+1)\frac{R}{2M}}\right)^{\kappa} a(f)^{\left(1-\frac{(m+1)R}{2M}\right)^{\varrho}}. \quad (9)$$

It is worth noting that for the case of multiple targets emitting different average transmission power P_l, $P_{l,\min}$ can be considered to guarantee that all targets' signals can be detected and the sensors can at least detect a nearby target. Accordingly, detectors in the farthest tier to a certain target will have decisions of 0. However, for a very large surveillance area it might be more efficient to divide the whole surveillance area into a number of $\tilde{m}$ non-overlapping subareas (e.g. clusters) and then each subarea is divided into M tiers, and accordingly the thresholds can be set as

$$\tau_{M-m-2}(\boldsymbol{\theta}) = P_{l,\min}\left(\frac{2\tilde{m}M}{(m+1)R}\right)^{\kappa} a(f)^{\left(1-\frac{(m+1)R}{2\tilde{m}M}\right)^{\varrho}}. \quad (10)$$

The last thresholding metric is more efficient in the case of multiple targets in terms of performance and power saving as $\tilde{m}$ might be selected to be in the order of the maximum number of potential targets.

IV. Decode-and-forward processing at CHDs

Sensors transmit their modulated data to the CHDs over Rician fading channels. Similar to RF communications, the acoustic signal transmitted from the underwater sensors to their CHD through water may reflect from the surface of the water, the bottom of the sea, or any other possible existing obstacles in the surroundings. In addition, the CHD is usually fixed on a buoy, which may fluctuate due to water waves [49], [50]. Thus, in this work we consider the Rician distribution to model both underwater acoustic and RF channels. Accordingly, the baseband representation of the signal received by the ith CHD that is sent by the sensor (i,k), i.e., the kth sensor in the ith cluster, can be expressed as

$$\tilde{y}_{i,k} = \sqrt{P_{\mathrm{s}}\mathcal{B}_i^k\left(\tilde{d}_i^k, \tilde{f}_{i,k}\right)}\tilde{h}_{i,k}u_{i,k}^{(m)} + \tilde{\varphi}_{i,k} \quad (11)$$

where P_{s} is the transmitted power for a sensor node, $\mathcal{B}_i^k\left(d_i^k, \tilde{f}_{i,k}\right)$ is the pathloss factor between CHD i and sensor k which can be evaluated using (1), $\tilde{d}_i^k$ is the distance, $\tilde{f}_{i,k}$ is the transmission frequency of the sensors, $\tilde{h}_{i,k} \sim \mathcal{CN}(m_{\tilde{h}}, 2\sigma_{\tilde{h}}^2)$ is a complex Gaussian distributed channel gain, and $\tilde{\varphi}_{i,k} \sim \mathcal{CN}(0, \sigma_{\tilde{\varphi}}^2)$ is AWGN.

At the CHDs, the decisions are decoded and then forwarded to the DCD. In this work, we use three types of detection schemes based on the availability of channel information at the receiver. First, CD is used to extract the data given complete knowledge about CSI. In the second type, ACD is

used for which the channel envelopes are only required at the receiver side, eliminating the need for the instantaneous phases. The third type is the NCED, which does not require the instantaneous knowledge about the channel, neither amplitudes nor phases [51], [57], [58].

A. Coherent Detection

Given perfect CSI with amplitude and phase knowledge at the receiver, the coherent maximum likelihood detector (cMLD) can be formulated as

$$\hat{u}_{i,k} = \arg \max_{u_{i,k}^{(m)} \in \mathcal{U}_k} f\left(\tilde{y}_{i,k} | \tilde{h}_{i,k}, u_{i,k}^{(m)}\right) \tag{12}$$

Given that $\tilde{y}_{i,k|\tilde{h}_{i,k},u_{i,k}^{(m)}} \sim \mathcal{CN}\left(\mu_{\tilde{y}_{i,k}}, 2\sigma_{\tilde{\varphi}}^2\right)$ with $\mu_{\tilde{y}_{i,k}} = \sqrt{P_{\mathrm{s}}\mathcal{B}_i^k\left(\tilde{d}_i^k, \tilde{f}_{i,k}\right)}\tilde{h}_{i,k}u_{i,k}^{(m)}$, the cMLD can be reduced to

$$\hat{u}_{i,k} = \arg \min_{u_{i,k}^{(m)} \in \mathcal{U}_k} \left| \tilde{y}_{i,k} - \sqrt{P_{\mathrm{s}}\mathcal{B}_i^k\left(\tilde{d}_i^k, \tilde{f}_{i,k}\right)} u_{i,k}^{(m)} \tilde{h}_{i,k} \right|, \tag{13}$$

After some algebraic manipulations, the cMLD can be expressed in a more convenient form as

$$z_{i,k} \underset{\hat{u}_{i,k}=u_{i,k}}{\overset{\hat{u}_{i,k}=\mathrm{u}_{i,k}}{\gtrless}} \frac{(\mathrm{u}_{i,k} + u_{i,k})}{2} \tag{14}$$

where $z_{i,k} \triangleq \frac{1}{\sqrt{P_{\mathrm{s}}\mathcal{B}_i^k\left(\tilde{d}_i^k, \tilde{f}_{i,k}\right)}|\tilde{h}_{i,k}|^2} \mathrm{Re}\left(\tilde{h}_{i,k}^* \tilde{y}_{i,k}\right)$. Consequently, the detection and decision regions can be formulated as

$$\hat{u}_{i,k,\mathrm{CD}} = \begin{cases} 0, & \tau_{-1} = -\infty < z_{i,k} < \tau_{\mathrm{CD},0} \\ 1, & \tau_{\mathrm{CD},0} \le z_{i,k} < \tau_{\mathrm{CD},1} \\ \vdots & \vdots \\ M-1, & \tau_{\mathrm{CD},M-2} \le z_{i,k} < \tau_{\mathrm{CD},M-1} = \infty \end{cases} \tag{15}$$

where $\tau_{\mathrm{CD},m} = \frac{1}{2}\left(u_{i,k}^{(m)} + u_{i,k}^{(m+1)}\right) \forall m$ are the detection thresholds. The complete derivations for the pairwise SER (SER) and symbol correct detection probability (SCDP) for this type of detection are provided in Appendix I.

B. Amplitude Coherent Detection

Although cMLD introduced in Sec. IV-A provides the optimal performance, the knowledge of the instantaneous envelopes and phases for all the Sensors-CHDs channels are required which might increase the complexity of the system and impose some limitations and challenges for large WSNs. Therefore, a semi-coherent, or more specifically, ACD, has been proposed in our previous work in [51], [57], [58], [61], which has also been investigated by other authors in the literature [62], [63]. ACD is only dependent on the channel envelope rather than complete CSI, which simplifies the receiver structure by eliminating the need of instantaneous phases knowledge. The amplitude coherent detector can be written as [51]

$$\hat{u}_{i,k} = \arg \min_{u_{i,k}^{(m)} \in \mathcal{U}_k} \left(\frac{|\tilde{y}_{i,k}|}{\tilde{\alpha}_{i,k}} - u_{i,k}^{(m)} \right)^2. \tag{16}$$

The detailed analysis for the correct and error detection probabilities for this type of detection can be found in [51].

C. Noncoherent energy detection

To avoid channel estimation overhead and simplify the receiver structure more, NCED can be applied at the destination. The first step is performed by evaluating the energy content in the received signal, which can be executed by using a simple envelope detector followed by a squaring device, which is mathematically expressed as $\tilde{r}_{i,k} = |\tilde{y}_{i,k}|^2$. Thereafter, the energy reading is compared to a set of thresholds to estimate the transmitted data symbol. To evaluate the optimum thresholds for this detection scheme, the distribution of $\tilde{r}_{i,k}$ is required. It can be noticed that $\tilde{y}_{i,k}|u_{i,k}^{(m)} \sim \mathcal{CN}\left(m_{\tilde{y}_{i,k}|u_{i,k}^{(m)}}, 2\sigma^2_{\tilde{y}_{i,k}|u_{i,k}^{(m)}}\right)$ with $m_{\tilde{y}_{i,k}|u_{i,k}^{(m)}} = \sqrt{P_{\mathrm{s}}\mathcal{B}_i^k\left(\tilde{d}_i^k, \tilde{f}_{i,k}\right)} u_{i,k}^{(m)} m_{\tilde{h}}$ and $\sigma^2_{\tilde{y}_{i,k}|u_{i,k}^{(m)}} = P_{\mathrm{s}}\mathcal{B}_i^k\left(\tilde{d}_i^k, \tilde{f}_{i,k}\right)\sigma_{\tilde{h}}^2\left(u_{i,k}^{(m)}\right)^2 + \sigma_{\tilde{\varphi}}^2$, and thus $\tilde{r}_{i,k}$ is a noncentral Chi-squared random variable with 2 degrees of freedom and a noncentrality parameter of $\mu_{\tilde{r}|u_{i,k}^{(m)}} = \sqrt{P_{\mathrm{s}}\mathcal{B}_i^k\left(\tilde{d}_i^k, \tilde{f}_{i,k}\right)\left(u_{i,k}^{(m)}\right)^2 \mu_{\tilde{h}}^2}$ when $u_{i,k} \in \{1, 2, \cdots, M-1\}$. However, when $u_{i,k} = 0$, $\tilde{y}_{i,k|u_{i,k}^{(m)}=0} \sim \mathcal{CN}\left(0, 2\sigma_{\tilde{\varphi}}^2\right)$ and thus the distribution of $\tilde{r}_{i,k}$ is Chi-squared with with 2 degrees of freedom. However, since the PDF of a noncentral Chi-squared distribution contains a modified Bessel function of the first kind and 0 order, deriving a closed-form formula for thresholds is not tractable. Therefore, the decision regions can be identified using a set of thresholds $\boldsymbol{\tau}_{\mathrm{NCED}} = [\tau_{\mathrm{NCED},0} = 0, \tau_{\mathrm{NCED},1}, \cdots, \tau_{\mathrm{NCED},M-1}, \tau_{\mathrm{NCED},M} = \infty]$ which are evaluated by using numerical tools such as Newton-Raphson and bi-section methods, and thus the decision decoding metric can be written as

$$\hat{u}_{i,k} = \begin{cases} 0, & 0 < |\tilde{y}_{i,k}|^2 < \tau_{\mathrm{NCED},1} \\ 1, & \tau_{\mathrm{NCED},1} \le |\tilde{y}_{i,k}|^2 < \tau_{\mathrm{NCED},2} \\ \vdots & \vdots \\ M-1, & \tau_{\mathrm{NCED},M-1} \le |\tilde{y}_{i,k}|^2 < \infty \end{cases}, \tag{17}$$

where $\tau_{\mathrm{NCED},m}$ is evaluated after finding the root of $f_{r_{i,k}}(r_{i,k}|u_m) - f_{r_{i,k}}(r_{i,k}|u_{m+1})$ numerically. The complete derivations for the PSER and SCDP for this type of detection are provided in Appendix II.

Fig. 4 presents a comparison between the introduced CD, ACD and NCED detection methods for different modulation orders M and different Rician factors $\mathcal{K}$. A point-to-point communication systems and a normalized pathloss are considered in this figure, and SNR is defined as $\mathrm{SNR} \triangleq P_{\mathrm{s}} / \sigma_{\tilde{\varphi}}^2$. As can be observed from the figure, a perfect match between the theoretical and simulation results is obtained, which confirms the correctness of the derivations carried out in this section for the error rates of CD and NCED. Besides, the subplots show a significant impact for $\mathcal{K}$ on SER where a higher $\mathcal{K}$ results in lower SER, for example, for the CD case with $M = 2$, SER at $\mathrm{SNR} = 14$ dB is approximately 3×10^{-2}, 2×10^{-4} and 1×10^{-6} when $\mathcal{K}$ equals 2 dB, 10 dB and 20 dB, respectively. The effect of increasing the modulation order M on SER is also clear from the figure, where increasing M generally degrades the SER performance, for instance, NCED suffers from an error floor when $M \ge 4$, whereas for CD, SER increases from 1×10^{-5} to 1×10^{-1} when M increases

from 2 to 8 at SNR $= 20$ dB and $\mathcal{K} = 10$ dB, as seen in Fig. 4.b. Moreover, the figure clearly shows that unlike NCED, ACD detection scheme does not suffer from an error floor regardless of M and its performance is mostly superior when compared to NCED and thus it is an excellent candidate when the channel phase is not known.

V. Locations Estimation at DCD

CHDs forward the decoded symbols to the DCD through interference-free channels, e.g., using TDMA, which are subject to Rician fading. Decisions received and collected by the DCD and then the location estimation process is carried out. Similar to the detection schemes employed at the CHDs, namely, CD, ACD and NCED, the estimation process at the DCD may be designed depending on the CSI availability at the DCD. It is worth mentioning that detection at the CHD and DCD can be different, for example, NCED and CD can be applied at the CHD and DCD, respectively. However, without loss of generality, we assume similar detection schemes are applied at both receiving ends for the sake of consistency and brevity. Nevertheless, considering different detection schemes at both communication ends is a straight-forward extension for the framework provided in this section. For the sake of clarity, we assume that the number of targets L is known at the DCD in this section, whereas the general solution with unknown number of targets is investigated in Sec. VI. The decision relayed by the CHD i, i.e., $\hat{u}_{i,k}$, is received at the DCD as

$$y_{i,k} = \sqrt{\tilde{P}_i \mathcal{B}_i^{\mathrm{c}}\left(d_i^{\mathrm{c}}, f_i^{\mathrm{c}}\right)}\hat{u}_{i,k} h_{i,k} + \varphi_{i,k} \tag{18}$$

where $\tilde{P}_i$ is the transmitted power of the ith CHD, $\mathcal{B}_i^{\mathrm{c}}\left(d_i^{\mathrm{c}}, f_i^{\mathrm{c}}\right)$ is the pathloss of the channel with d_i^{c} and f_i^{c} respectively denote the distance from the ith CHD to the DCD and the transmission signal frequency, $h_i \sim \mathcal{CN}(m_h, 2\sigma_h^2)$ is a complex Gaussian distributed channel gain, and $\varphi_{i,k} \sim \mathcal{CN}(0, \sigma_\varphi^2)$ is AWGN. It is worth highlighting that the transmission employed at the CHDs to send their decoded data to the DCD is performed using RF signals even in underwater localization scenario as the CHDs are typically attached to buoys communicating with a ground station or UAV. The joint PDF of $\mathbf{Y} \in \mathbb{C}^{C \times K_{\mathrm{c}}} = [\mathbf{y}_1, \mathbf{y}_2, \ldots, \mathbf{y}_C]^T$ with $\mathbf{y}_i = [y_{i,1}, y_{i,2}, \ldots, y_{i,K_{\mathrm{c}}}]$, conditioned on the vector of unknown parameters $\boldsymbol{\theta} \in \mathbb{C}^{1\times 3L}$ and given the number of targets L is dependent on the CSI availability and detection method considered at the DCD. Nevertheless, it can be generally represented as

$$f\left(\mathbf{Y}|\boldsymbol{\Xi}, \boldsymbol{\theta}\right) = \prod_{i=1}^{C}\prod_{k=1}^{K_{\mathrm{c}}} f\left(y_{i,k}|\boldsymbol{\theta}, \Xi_{i,k}\right) \tag{19}$$

where $\Xi_{i,k} \in \{h_{i,k}, \alpha_{i,k}\}$ for the cases of CD and ACD, respectively, whereas the PDF is independent of $\boldsymbol{\Xi}$ when NCED is applied. After employing the law of total probability, $f\left(\mathbf{Y}|\boldsymbol{\Xi}, \boldsymbol{\theta}\right)$ can be written as

$$f\left(\mathbf{Y}|\boldsymbol{\Xi},\boldsymbol{\theta}\right) = \prod_{i=1}^{C}\prod_{k=1}^{K_{\mathrm{c}}} \sum_{\hat{u}_{i,k}\in\mathcal{U}_k}\sum_{u_{i,k}\in\mathcal{U}_k} f\left(y_{i,k}|\hat{u}_{i,k}, \Xi_{i,k}\right) \times \Pr\left(\hat{u}_{i,k}|u_{i,k}\right)\Pr\left(u_{i,k}|\boldsymbol{\theta}\right) \tag{20}$$

where $\Pr\left(\hat{u}_{i,k}|u_{i,k}\right)$ is PSER or SCDP for the Sensors-CHDs links, which has been derived in Sec. IV, and $\Pr\left(u_{i,k}|\boldsymbol{\theta}\right)$ is the quantized decision statistics in (7). Consequently, the optimal estimator can be constructed as (21) on page 10. It is worth noting that analytical solution for $\boldsymbol{\theta}$ may not be feasible because the partial derivatives of the objective function in (21) are not solvable, and thus an optimization tool is required to find $\boldsymbol{\theta}$ that maximizes $\mathcal{L}_{\mathrm{CD,opt}}\left(\boldsymbol{\theta}\right)$. Among many possible optimization tools candidates, the Genetic algorithm (GA) is adopted in this paper.

For the complete CSI knowledge scenario, i.e., CD, it can be easily proven that the PDF $f\left(y_{i,k}|\hat{u}_{i,k}, \Xi_{i,k}\right)$ is $\mathcal{CN}\left(\sqrt{\tilde{P}_i \mathcal{B}_i^{\mathrm{c}}\left(d_i^{\mathrm{c}}, f_i^{\mathrm{c}}\right)}\hat{u}_{i,k}\Xi_{i,k}, 2\sigma_\varphi^2\right)$ with $\Xi_{i,k} = h_{i,k}$. To find the PDF under the availability of channel amplitudes only, i.e., ACD case, we first rewrite $f\left(y_{i,k}|h_{i,k}, \hat{u}_{i,k}\right)$ as

$$f\left(y_{i,k}|\alpha, \phi_h, \hat{u}_{i,k}\right) = \frac{1}{2\pi\sigma_\varphi^2}\exp\left(-\frac{|y_{i,k}|^2 + \tilde{P}_i\mathcal{B}_i^{\mathrm{c}}(d_i^{\mathrm{c}}, f_i^{\mathrm{c}})\alpha^2\hat{u}_{i,k}^2}{2\sigma_\varphi^2}\right) \times \exp\left(\frac{\sqrt{\tilde{P}_i \mathcal{B}_i^{\mathrm{c}}\left(d_i^{\mathrm{c}}, f_i^{\mathrm{c}}\right)}\alpha\hat{u}_{i,k}}{\sigma_\varphi^2}|y_{i,k}|\cos\left(\phi_y - \phi_h\right)\right) \tag{22}$$

where $\phi_y = \arctan\left(\frac{y_{i,k,\Im}}{y_{i,k,\Re}}\right)$ is the phase of the received signal $y_{i,k}$ with $y_{i,k,\Im} \triangleq \mathrm{Im}\left(y_{i,k}\right)$ and $y_{i,k,\Re} \triangleq \mathrm{Re}\left(y_{i,k}\right)$. As can be seen from (18) that at significant SNR, the noise term can be neglected and thus $\phi_y \to \phi_h$ since transmitted symbols are real valued. By following this fact, it can be interpreted that $\cos\left(\phi_y - \phi_h\right) \longrightarrow 1$ and thus $f\left(y_{i,k}|\alpha, \phi_h, \hat{u}_{i,k}\right)$ at high SNR can be approximated as

$$f\left(y_{i,k}|\Xi_{i,k}, \hat{u}_{i,k}\right) \approx \frac{\exp\left(-\frac{\left(|y_{i,k}| - \sqrt{\tilde{P}_i\mathcal{B}_i^{\mathrm{c}}\left(d_i^{\mathrm{c}}, f_i^{\mathrm{c}}\right)}\Xi_{i,k}\hat{u}_{i,k}\right)^2}{2\sigma_\varphi^2}\right)}{2\pi\sigma_\varphi^2} \tag{23}$$

with $\Xi_{i,k} = \alpha_{i,k}$ in the case of ACD. Finally, the energy readings $r_{i,k} = |y_{i,k}|^2$ are considered in NCED scenario and thus $f\left(r_{i,k}|\hat{u}_{i,k} = 0\right)$ can be found as a Chi-squared distribution with 2 degrees of freedom, i.e., exponential distribution with a rate parameter of $\frac{1}{2\sigma_\varphi^2}$, whose PDF is given by

$$f\left(r_{i,k}|\hat{u}_{i,k} = 0\right) = \frac{1}{2\sigma_\varphi^2}\exp\left(-\frac{r_{i,k}}{2\sigma_\varphi^2}\right), \tag{24}$$

whereas $f\left(r_{i,k}|\hat{u}_{i,k} > 0\right)$ is a noncentral Chi-squared PDF given by

$$f\left(r_{i,k}|\hat{u}_{i,k} > 0\right) = \frac{\exp\left(-\frac{r_{i,k} + \varkappa^2}{2\sigma^2_{y_{i,k}|\hat{u}_{i,k}}}\right)}{2\sigma^2_{y_{i,k}|\hat{u}_{i,k}}} I_0\left(\frac{\varkappa\sqrt{r_{i,k}}}{\sigma^2_{y_{i,k}|\hat{u}_{i,k}}}\right), \tag{25}$$

where $\sigma^2_{y_{i,k}|\hat{u}_{i,k}} = \tilde{P}_i\mathcal{B}_i^{\mathrm{c}}\left(d_i^{\mathrm{c}}, f_i^{\mathrm{c}}\right)\sigma_h^2\hat{u}_{i,k}^2 + \sigma_\varphi^2$ and $\varkappa = \sqrt{\tilde{P}_i\mathcal{B}_i^{\mathrm{c}}\left(d_i^{\mathrm{c}}, f_i^{\mathrm{c}}\right)\hat{u}_{i,k}^2\mu_h^2}$.

1) Decode-then-estimate (Hard decoding): In the high SNR regime, the receiver can extract the original transmitted decisions with a very low probability of error. In such a case, the estimator can be separated into two stages. In the first stage, data detection is used to extract the transmitted decisions, thereafter in the second stage, the extracted decisions $\breve{u}_{i,k}$ are sent to a ML estimator to estimate the locations of targets, and thus we refer this estimator as DTE. For the decoding stage, similar detectors to those designed in Sec. IV for detecting data at the CHDs, e.g. CD, ACD and NCED, can be employed

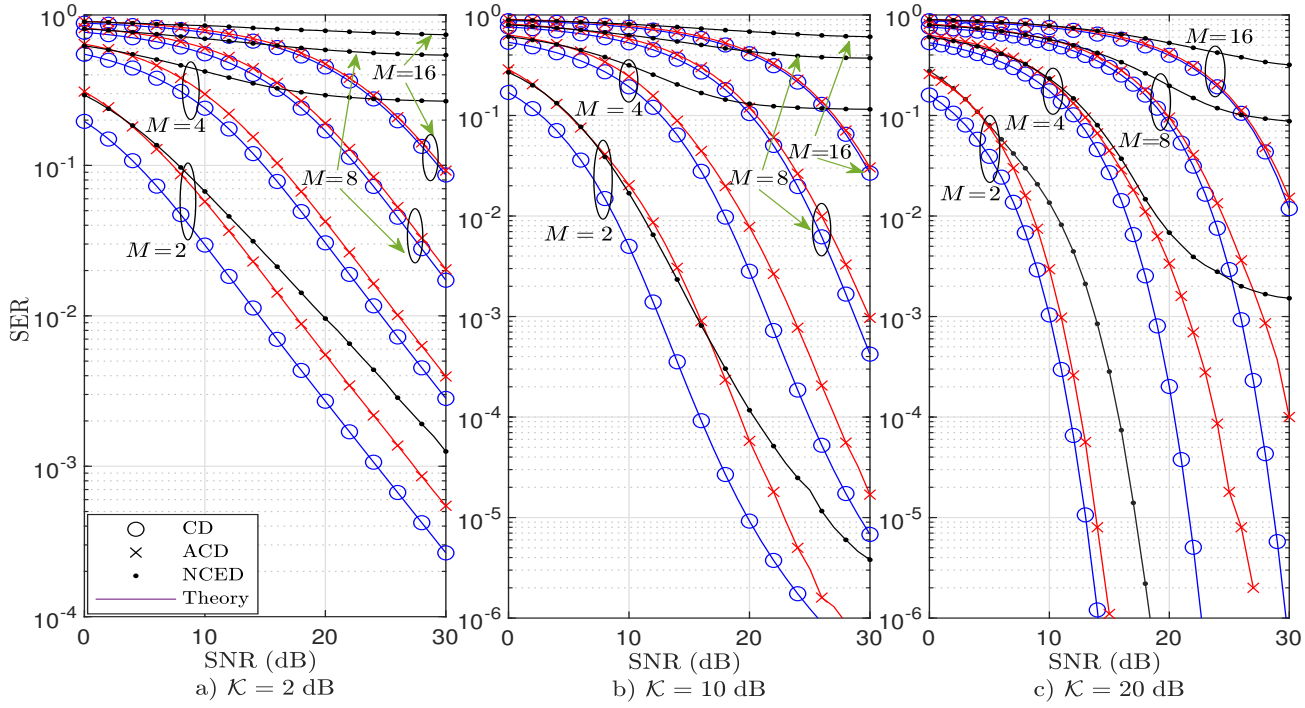

Fig. 4. The achievable SER for CD, ACD and NED detection schemes.

$$\hat{\boldsymbol{\theta}} = \arg\max_{\boldsymbol{\theta}} \underbrace{\sum_{i=1}^{C}\sum_{k=1}^{K_c} \ln\left\{ \sum_{\hat{u}_{i,k}\in\mathcal{U}_k} \sum_{u_{i,k}\in\mathcal{U}_k} f\left(y_{i,k}|\hat{u}_{i,k},\Xi_{i,k}\right) \Pr\left(\hat{u}_{i,k}|u_{i,k}\right) \Pr\left(u_{i,k}|\boldsymbol{\theta}\right) \right\}}_{\mathcal{L}_{\text{opt.}}(\boldsymbol{\theta})} \tag{21}$$

at the DCD as well, and thus there is no need to rewrite the formulas and descriptions for the sake of brevity. After detecting the data symbols, the MLE applied in the second stage is based on the statistics of $\check{u}_{i,k}\forall\{i,k\}$ and can be expressed as

$$\mathcal{L}_{\text{DTE}}\left(\boldsymbol{\theta}\right) = \sum_{i=1}^{C}\sum_{k=1}^{K_c} \ln \Pr\left(\check{u}_{i,k}|\boldsymbol{\theta}\right) \tag{26}$$

By using the law of total probability, $\mathcal{L}_{\text{DTE}}\left(\boldsymbol{\theta}\right)$ can be expanded to (27) on page 11, where $\mathbb{U}_k^c \in \mathbb{C}^{1\times M(M-1)}$ is a set of all possible pairs of $\{\hat{u}_{i,k},u_{i,k}\}\forall\{\hat{u}_{i,k}\neq\check{u}_{i,k}\cup\check{u}_{i,k}\neq u_{i,k}\}$. Interestingly, p_1 and p_2 represent the pairwise correct probability for the Sensor-CHD and CHD-DCD links, respectively, while p_3p_4 represents the probability of having errors in one or both links, and thus $p_3p_4 \ll p_1p_2$ at considerable SNR. Consequently, by neglecting the decoding errors at the CHDs and DCD, $\mathcal{L}_{\text{DTE}}\left(\boldsymbol{\theta}\right)$ reduces to

$$\tilde{\mathcal{L}}_{\text{DTE}}(\boldsymbol{\theta}) = \sum_{i=1}^{C}\sum_{k=1}^{K_c} \ln\left(Q\left(\frac{\check{\tau}_{m-1}-\mu_{s_k}(\boldsymbol{\theta})}{\sigma_{s_k}\left(\boldsymbol{\theta}\right)}\right) - Q\left(\frac{\check{\tau}_{m}-\mu_{s_k}(\boldsymbol{\theta})}{\sigma_{s_k}\left(\boldsymbol{\theta}\right)}\right)\right) \tag{28}$$

where $\{\check{\tau}_{m-1},\check{\tau}_m\}$ are the thresholds associated with the detected decision $\check{u}_{i,k}$, i.e., $\check{\tau}_{m-1}\leq\check{z}_{i,k}<\check{\tau}_m \longmapsto \check{u}_{i,k}=u_{i,k}^{(m)}$.

By comparing (28) with (21), it can be realized that the complexity of DTE location estimator is relatively low as the exponential terms have been totally avoided and the inner double-summation in (21) has been omitted. This simplification will be at the expense of the localization accuracy, however, the performance of both estimators is expected to converge at high SNR.

VI. PMLE WITH UNKNOWN L

In Sec. V, the number of targets L is assumed to be known at the DCD, however, this assumption may not be valid in several practical scenarios in which there is a persistent need to estimate the number of targets in addition to their locations. Therefore, a penalty term, also called a regularization term, which is a function of the number of targets L can be added to the likelihood function to infer the number of targets. Different information criteria are proposed to penalize the likelihood function according to the number of estimated parameters, i.e., AIC, cAIC, BIC and HQIC. It is worth mentioning that BIC, cAIK and HQIC in general favor models with less parameters, i.e., less number of targets, which helps in avoiding overfitting problems. Moreover, while they serve a similar purpose, there is a difference in how the penalty term is calculated. For instance, BIC incorporates a penalty for model complexity stronger than AIC, whereas HQIC seeks to balance the trade-off between the goodness of fit and model complexity. PMLE can be generally expressed by [64]

$$\mathcal{L}_{\mathrm{DTE}}\left(\boldsymbol{\theta}\right)=\sum_{i=1}^{C}\sum_{k=1}^{K_{\mathrm{c}}}\ln\left\{\sum_{\hat{u}_{i,k}\in\mathcal{U}_k}\sum_{u_{i,k}\in\mathcal{U}_k}\Pr\left(\check{u}_{i,k}|\hat{u}_{i,k}\right)\Pr\left(\hat{u}_{i,k}|u_{i,k}\right)\Pr\left(u_{i,k}|\boldsymbol{\theta}\right)\right\}$$
$$=\sum_{i=1}^{C}\sum_{k=1}^{K_{\mathrm{c}}}\ln\left\{\underbrace{\Pr\left(\check{u}_{i,k}=\hat{u}_{i,k}|\hat{u}_{i,k}\right)}_{p_1}\underbrace{\Pr\left(\hat{u}_{i,k}=u_{i,k}|u_{i,k}\right)}_{p_2}\Pr\left(u_{i,k}|\boldsymbol{\theta}\right)+\sum_{\mathbb{U}_k^{\mathrm{c}}}\underbrace{\Pr\left(\check{u}_{i,k}|\hat{u}_{i,k}\right)}_{p_3}\underbrace{\Pr\left(\hat{u}_{i,k}|u_{i,k}\right)}_{p_4}\Pr\left(u_{i,k}|\boldsymbol{\theta}\right)\right\} \quad (27)$$

$$\left[\hat{L}_{\mathrm{pen}},\hat{\boldsymbol{\theta}}_{\mathrm{pen}}\right]=\arg\max_{L,\boldsymbol{\theta}}2\mathcal{L}_{\mathrm{est}}\left(\boldsymbol{\theta}\right)-\mathcal{T}_{\mathrm{pen}} \quad (29)$$

where the subscript $(\cdot)_{\mathrm{est}}$ refers to any of the estimators introduced in Sec. V, i.e., est $\in\{\mathrm{CD},\mathrm{ACD},\mathrm{NCED},\mathrm{DTE}\}$, and $\mathcal{T}_{\mathrm{pen}}\in\left\{3L\ln\left(K\right),\ 6L,\ \frac{6LK}{K-3L-1},\ 6L\log\left(\log K\right)\right\}$ are typically used for $\{$BIC, AIC, cAIC, HQIC$\}$, respectively. It is important to note that there is no specific preference for one criterion over the others, and therefore we employ all these criteria in this work to test their functionality to solve the problem of estimating the number of targets.

VII. CRLB

CRLB theorem is a bound that is typically used to measure the efficiency of unbiased estimators. More specifically, the variance of an unbiased estimator is bounded by the inverse of FIM, i.e., $\mathbf{F}^{-1}$. Mathematically, CRLB can be written as [65],

$$\mathbb{E}\left[\left(\hat{\boldsymbol{\theta}}_{\mathrm{est}}-\boldsymbol{\theta}\right)\left(\hat{\theta}_{\mathrm{est}}-\boldsymbol{\theta}\right)^{H}\right]\geq\mathbf{F}_{\mathrm{est}}^{-1} \quad (30)$$

where $(\cdot)^H$ is the Hermitian operator, and $\mathbb{E}\left[\cdot\right]$ is the expectation operation. For a number of L targets each of which has 3 parameters to estimate, i.e., its Cartesian coordinates (x_l,y_l,z_l), the FIM can be written as

$$\mathbf{F}_{\mathrm{est}}\triangleq\mathbb{E}\left[-\nabla_{\boldsymbol{\theta}}\left(\nabla_{\boldsymbol{\theta}}\right)^{t}\left(\mathcal{L}_{\mathrm{est}}\left(\boldsymbol{\theta}\right)\right)\right]=-\mathbb{E}\begin{bmatrix}\mathbf{F}_{1,1}\cdots\mathbf{F}_{1,L}\\ \vdots\quad\ddots\quad\vdots\\ \mathbf{F}_{L,1}\cdots\mathbf{F}_{L,L}\end{bmatrix} \quad (31)$$

where $\nabla_{\boldsymbol{\theta}}$ and $(\cdot)^t$ are the gradient and transpose operators, respectively, and $\mathbf{F}_{l,l}$ and $\mathbf{F}_{l,\acute{l}}$ can be expressed as

$$\mathbf{F}_{l,l}=\begin{bmatrix}\frac{\partial^2\mathcal{L}_{\mathrm{est}}(\boldsymbol{\theta})}{\partial x_l^2} & \frac{\partial^2\mathcal{L}_{\mathrm{est}}(\boldsymbol{\theta})}{\partial x_l\partial y_l} & \frac{\partial^2\mathcal{L}_{\mathrm{est}}(\boldsymbol{\theta})}{\partial x_l\partial z_l}\\ \frac{\partial^2\mathcal{L}_{\mathrm{est}}(\boldsymbol{\theta})}{\partial x_l\partial y_l} & \frac{\partial^2\mathcal{L}_{\mathrm{est}}(\boldsymbol{\theta})}{\partial y_l^2} & \frac{\partial^2\mathcal{L}_{\mathrm{est}}(\boldsymbol{\theta})}{\partial y_l\partial z_l}\\ \frac{\partial^2\mathcal{L}_{\mathrm{est}}(\boldsymbol{\theta})}{\partial x_l\partial z_l} & \frac{\partial^2\mathcal{L}_{\mathrm{est}}(\boldsymbol{\theta})}{\partial y_l\partial z_l} & \frac{\partial^2\mathcal{L}_{\mathrm{est}}(\boldsymbol{\theta})}{\partial z_l^2}\end{bmatrix}, \quad (32)$$

$$\mathbf{F}_{l,\acute{l}}=\begin{bmatrix}\frac{\partial^2\mathcal{L}_{\mathrm{est}}(\boldsymbol{\theta})}{\partial x_l\partial x_{\acute{l}}} & \frac{\partial^2\mathcal{L}_{\mathrm{est}}(\boldsymbol{\theta})}{\partial x_l\partial y_{\acute{l}}} & \frac{\partial^2\mathcal{L}_{\mathrm{est}}(\boldsymbol{\theta})}{\partial x_l\partial z_{\acute{l}}}\\ \frac{\partial^2\mathcal{L}_{\mathrm{est}}(\boldsymbol{\theta})}{\partial x_l\partial y_{\acute{l}}} & \frac{\partial^2\mathcal{L}_{\mathrm{est}}(\boldsymbol{\theta})}{\partial y_l\partial y_{\acute{l}}} & \frac{\partial^2\mathcal{L}_{\mathrm{est}}(\boldsymbol{\theta})}{\partial y_l\partial z_{\acute{l}}}\\ \frac{\partial^2\mathcal{L}_{\mathrm{est}}(\boldsymbol{\theta})}{\partial x_l\partial z_{\acute{l}}} & \frac{\partial^2\mathcal{L}_{\mathrm{est}}(\boldsymbol{\theta})}{\partial y_l\partial z_{\acute{l}}} & \frac{\partial^2\mathcal{L}_{\mathrm{est}}(\boldsymbol{\theta})}{\partial z_l\partial z_{\acute{l}}}\end{bmatrix}, \quad (33)$$

for which $l\in\{1,2,\cdots,L\}$ and $l\neq\acute{l}$. However, for the sake of brevity, we provide the detailed analysis for the FIM of the optimal estimator with CD provided in (21) with $\Xi_{i,k}=h_{i,k}$. Similar steps can be followed to derive the FIM of the other estimators. Consequently, by referring to $\mathcal{L}_{\mathrm{CD,opt}}\left(\boldsymbol{\theta}\right)$ provided in (21), it can be realized that the first and second partial derivatives of $\mathcal{L}_{\mathrm{CD,opt}}\left(\boldsymbol{\theta}\right)$ with respect to $\chi_l\in\{x_l,y_l,z_l\}$ can be respectively given by

$$\frac{\partial\mathcal{L}_{\mathrm{c,opt}}\left(\boldsymbol{\theta}\right)}{\partial\chi_l}=\sum_{i=1}^{C}\sum_{k=1}^{K_{\mathrm{c}}}\frac{\frac{\partial}{\partial\chi_l}f\left(y_{i,k}|\boldsymbol{\theta}\right)}{f\left(y_{i,k}|\boldsymbol{\theta}\right)}, \quad (34)$$

and

$$\frac{\partial^2\mathcal{L}_{\mathrm{c,opt}}(\boldsymbol{\theta})}{\partial\chi_l^2}=\sum_{i=1}^{C}\sum_{k=1}^{K_{\mathrm{c}}}\frac{f\left(y_{i,k}|\boldsymbol{\theta}\right)\frac{\partial^2}{\partial\chi_l^2}f\left(y_{i,k}|\boldsymbol{\theta}\right)-\left(\frac{\partial}{\partial\chi_l}f\left(y_{i,k}|\boldsymbol{\theta}\right)\right)^2}{\left(f\left(y_{i,k}|\boldsymbol{\theta}\right)\right)^2} \quad (35)$$

where $\partial^2\mathcal{L}_{\mathrm{c,opt}}\left(\boldsymbol{\theta}\right)/\partial\chi_l^2$ is used to evaluate the main diagonal entries of $\mathbf{F}_{\mathrm{est}}$. Subsequently, evaluating the negative of the expected value of $\partial^2\mathcal{L}_{\mathrm{c,opt}}\left(\boldsymbol{\theta}\right)/\partial\chi_l^2$, i.e., $-\mathbb{E}\left[\partial^2\mathcal{L}_{\mathrm{c,opt}}\left(\boldsymbol{\theta}\right)/\partial\chi_l^2\right]$, and noting that $\mathbb{E}\left[\frac{\partial^2}{\partial\chi_l^2}f\left(y_{i,k}|\boldsymbol{\theta}\right)\ /\ f\left(y_{i,k}|\boldsymbol{\theta}\right)\right]=0$, we obtain

$$-\mathbb{E}\left[\frac{\partial^2\mathcal{L}_{\mathrm{c,opt}}\left(\boldsymbol{\theta}\right)}{\partial\chi_l^2}\right]=\sum_{i=1}^{C}\sum_{k=1}^{K_{\mathrm{c}}}\int_{-\infty}^{\infty}\frac{\left(\frac{\partial}{\partial\chi_l}f\left(y_{i,k}|\boldsymbol{\theta}\right)\right)^2}{f\left(y_{i,k}|\boldsymbol{\theta}\right)}dy_{i,k}. \quad (36)$$

Therefore, $f\left(y_{i,k}|\boldsymbol{\theta}\right)$ and $\frac{\partial}{\partial\chi_l}f\left(y_{i,k}|\boldsymbol{\theta}\right)$ are needed to evaluate the FIM. To begin, the definition of $f\left(y_{i,k}|\boldsymbol{\theta}\right)$ provided in (20) is invoked, however, $f\left(y_{i,k}|\hat{u}_{i,k}\right)$ should be evaluated first by averaging the PDF of $f\left(y_{i,k}|\hat{u}_{i,k},h_{i,k}\right)$ over the distribution of $h_{i,k}$. Nevertheless, it can be observed that by performing phase equalization at the DCD, $\acute{y}_{i,k}\triangleq y_{i,k}\mathrm{e}^{j\phi_{i,k}}=\sqrt{\tilde{P}_i\mathcal{B}_i^{\mathrm{c}}\left(d_i^{\mathrm{c}},f_i^{\mathrm{c}}\right)}\hat{u}_{i,k}\alpha_{i,k}+\acute{\varphi}_{i,k}$, where $\acute{\varphi}_{i,k}=\varphi_{i,k}\mathrm{e}^{j\phi_{i,k}}\sim\mathcal{CN}\left(0,2\sigma_{\varphi}^2\right)$, the information is totally contained in the real part of $\acute{y}_{i,k}$. Consequently, the sufficient statistics of the received signal can be realized by $\breve{y}_{i,k}\triangleq\mathrm{Re}\left(\acute{y}_{i,k}\right)\sim\mathcal{N}\left(\sqrt{\tilde{P}_i\mathcal{B}_i^{\mathrm{c}}\left(d_i^{\mathrm{c}},f_i^{\mathrm{c}}\right)}\hat{u}_{i,k}\alpha_{i,k},\sigma_{\varphi}^2\right)$. Consequently, $f\left(y_{i,k}|\boldsymbol{\theta}\right)$ can be equivalently replaced by $f\left(\breve{y}_{i,k}|\boldsymbol{\theta}\right)$ which can be expressed as

$$f\left(\breve{y}_{i,k}|\boldsymbol{\theta}\right)=\sum_{\hat{u}_{i,k}}\sum_{u_{i,k}}f(\breve{y}_{i,k}|\hat{u}_{i,k})\Pr(\hat{u}_{i,k}|u_{i,k})\Pr(u_{i,k}|\boldsymbol{\theta}), \quad (37)$$

where the complete derivations for $f\left(\breve{y}_{i,k}|\hat{u}_{i,k}\right)$ and its partial derivative are provided in Appendix III.

After that, we substitute (61) and (60) in (59) which is then substituted in (57) to obtain $\frac{\partial}{\partial\chi_l}f\left(\breve{y}_{i,k}|\boldsymbol{\theta}\right)$, thereafter substituting the resulted $\frac{\partial}{\partial\chi_l}f\left(\breve{y}_{i,k}|\boldsymbol{\theta}\right)$ and $f\left(\breve{y}_{i,k}|\boldsymbol{\theta}\right)$ given by (37) in (36) yields

$$\mathbf{F}_{3l-2,3l-2}=\frac{1}{2\pi}\sum_{i=1}^{C}\sum_{k=1}^{K_{\mathrm{c}}}\beta^2\left(\boldsymbol{\theta}_l\right)\left(x_k-x_l\right)^2\mathcal{I}_{i,k}^{\mathrm{est}} \quad (38)$$

where

$$\mathcal{I}_{i,k}^{\mathrm{est}}=\int_{-\infty}^{\infty}\frac{\left(\sum_{\hat{u}_{i,k}}\sum_{u_{i,k}}f(\breve{y}_{i,k}|\hat{u}_{i,k})\Pr(\hat{u}_{i,k}|u_{i,k})\mathcal{B}_m(\boldsymbol{\theta})\Psi(\boldsymbol{\theta})\right)^2}{\sum_{\hat{u}_{i,k}}\sum_{u_{i,k}}f(\breve{y}_{i,k}|\hat{u}_{i,k})\Pr(\hat{u}_{i,k}|u_{i,k})\Pr\left(u_{i,k}|\boldsymbol{\theta}\right)}d\breve{y}_{i,k}, \quad (39)$$

which can be evaluated numerically, for example, trapezoidal integration method. Similar steps can be performed to derive

$$\mathbf{F}_{3l-1,3l-1}=\frac{1}{2\pi}\sum_{i=1}^{C}\sum_{k=1}^{K_{\mathrm{c}}}\beta^2\left(\boldsymbol{\theta}_l\right)\left(y_k-y_l\right)^2\mathcal{I}_{i,k}^{\mathrm{est}}, \quad (40)$$

and

$$\mathbf{F}_{3l,3l} = \frac{1}{2\pi}\sum_{i=1}^{C}\sum_{k=1}^{K_c}\beta^2\left(\boldsymbol{\theta}_l\right)\left(z_k - z_l\right)^2\mathcal{I}_{i,k}^{\text{est}}. \quad (41)$$

To evaluate the off-diagonal entries of $\mathbf{F}_{l,l}$, a similar procedure can be followed, which yields

$$\mathbf{F}_{3l-2,3l-1} = \frac{1}{2\pi}\sum_{i=1}^{C}\sum_{k=1}^{K_c}\beta^2\left(\boldsymbol{\theta}_l\right)\left(x_k - x_l\right)\left(y_k - y_l\right)\mathcal{I}_{i,k}^{\text{est}} \quad (42)$$

$$\mathbf{F}_{3l-2,3l} = \frac{1}{2\pi}\sum_{i=1}^{C}\sum_{k=1}^{K_c}\beta^2\left(\boldsymbol{\theta}_l\right)\left(x_k - x_l\right)\left(z_k - z_l\right)\mathcal{I}_{i,k}^{\text{est}} \quad (43)$$

$$\mathbf{F}_{3l-1,3l} = \frac{1}{2\pi}\sum_{i=1}^{C}\sum_{k=1}^{K_c}\beta^2\left(\boldsymbol{\theta}_l\right)\left(y_k - y_l\right)\left(z_k - z_l\right)\mathcal{I}_{i,k}^{\text{est}}. \quad (44)$$

Eventually, the elements of $\mathbf{F}_{l,\acute{l}}$ can be evaluated in a similar way and the final expressions are included in Table III.

VIII. Simulation Results

The simulation results for the multiple target localization problem illustrated in this paper are presented in this section, where Monte Carlo simulation is used with 1000 runs for each simulation point. GA with a population size of 50, a crossover fraction of 0.8, and maximum generations of 400 is applied to optimize the log-likelihood function $\mathcal{L}\left(\boldsymbol{\theta}\right)$. Sensors with known locations are uniformly distributed over a 2D grid with dimensions of $(400\text{ m} \times 400\text{ m})$ and divided into $C = 4$ clusters with equal size. Besides, the CHDs are placed at positions $(-100, -100, 50)$ m, $(-100, 100, 50)$ m, $(100, -100, 50)$ m and $(-100, 100, 50)$ m, as well as, the DCD is placed at $(0, 0, 100)$ and thus it has equal distance to the CHDs (e.g. $\mathcal{B}_i^{\text{c}}\left(d_i^{\text{c}}, f_i^{\text{c}}\right) = \mathcal{B}^{\text{c}}\left(d^{\text{c}}, f_i^{\text{c}}\right)\forall i$). The RMSE in the estimated location of the lth target is defined as $\text{RMSE}_l \triangleq \sqrt{\mathbb{E}\left[\left(x_l - \hat{x}_l\right)^2 + \left(y_l - \hat{y}_l\right)^2 + \left(z_l - \hat{z}_l\right)^2\right]}$. Unless otherwise stated, $L = 2$ targets are considered in our simulations, where these targets are denoted as l_1 and l_2, and they are placed at fixed location, i.e., $l_1 \sim (-50, 23, 0)$ m and $l_2 \sim (90, -135, 0)$ m. The emitted power from all targets, sensors and CHDs is fixed at $P_l = P_{\text{s}} = \tilde{P}_i = 0$ dB, the SNR for Sensors-CHDs links is defined as $\gamma_{\text{S-CHD}} \triangleq \frac{C}{K}\sum_i \frac{P_{\text{s}}\mathcal{B}_i^k\left(\tilde{d}_i^k, \tilde{f}_{k,i}\right)}{\sigma_{\tilde{\varphi}}^2}$, and the SNR for CHDs-DCD links is defined as $\text{SNR} \triangleq \frac{\tilde{P}_i\mathcal{B}^{\text{c}}\left(d^{\text{c}}, f_i^{\text{c}}\right)}{\sigma_{\tilde{\varphi}}^2}$. The transmission frequency for all RF links is fixed at 1 GHz, whereas it is fixed at 100 kHz for UW acoustic communications. Table IV conclude the parameters used for the simulation environment.

The RMSE in the location estimates of each target is presented in Fig. 5 for the optimal estimator with CD against the SNR of CHDs-DCD link. A number of 225 sensors are distributed in the environment and the SNR from the nearest sensor to its CHD is set to 35 dB, whereas different values for the modulation order M are considered. The figure also shows CRLB to provide the performance limit of the proposed estimator, as well as another widely used localization method referred to equalization-clustering-centroid (ECC) in order to provide another benchmark for the obtained RMSE [68]–[70]. It is worth noting that evaluating the centroid of sensors' locations is widely used in the literature of localization using WSNs; however, equalization and clustering stages have been

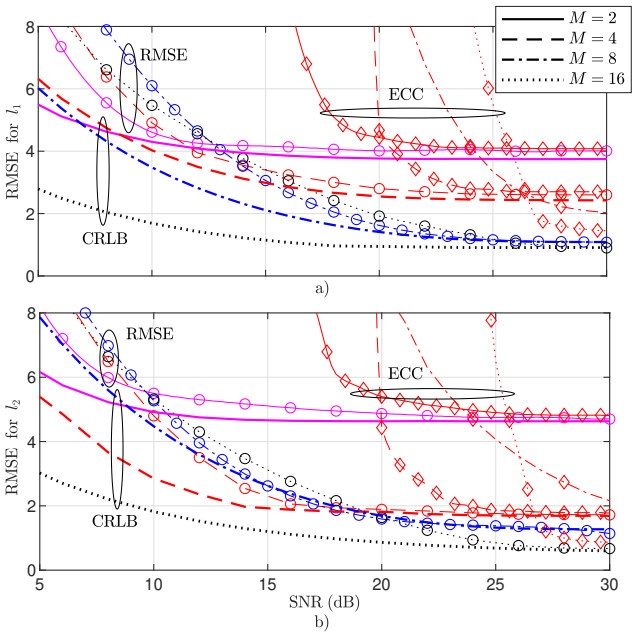

Fig. 5. The RMSE for each target for MLE-CD-Opt estimator under different values of M, where $K = 225$ and $\gamma_{\text{S-CHD}} = 35$ dB.

added before calculating the centroids due to channel imperfections and multiple target scenario which have been taken into account in this work. The results in Fig. 5 obviously show a superiority for the proposed MLE-CD-Opt estimator over ECC; although at very high SNR, ECC may approach MLE-CD-Opt in some cases. Moreover, MLE-CD-Opt approaches the performance limit obtained by CRLB at high SNR. It can be also seen that at low SNR, low quantization levels, i.e., low values for M, could provide better performance than large M. This behavior can be attributed to the fact that SER is generally directly proportional to the modulation order M, and thus symbols transmission suffers from considerable SER with large M and low SNR. However, the RMSE performance at high SNR is significantly lower with high M since errors produced by the channel become very low, and thus RMSE is dominated by the quantization errors and decreases as M increases.

Fig. 6 presents the achievable RMSE for MLE-CD-Opt against the SNR of CHDs-DCD channel, i.e., $\gamma_{\text{S-CHD}}$, and for different SNRs for Sensors-CHDs channels. The total number of distributed sensors and the modulation order are fixed at 225 and 8, respectively. It is noteworthy to mention that the curves for the ECC algorithm with $\gamma_{\text{S-CHD}} = \{5, 15\}$ dB are not shown in the figure because the achievable RMSE in these cases is very large, more than 40 m, and the obtained CRLB at $\gamma_{\text{S-CHD}} = 25$ dB is not shown as it is almost equal to CRLB at $\gamma_{\text{S-CHD}} = 35$ dB. As can be observed from the figure, Sensors-CHDs link has also a significant impact on the achievable RMSE, for example, when $\gamma_{\text{S-CHD}}$ is 5 dB, the lowest RMSE for estimating the locations of targets l_1 and l_2 is approximately 15 m and 10 m, respectively, when MLE-CD-Opt estimator is employed. Therefore, poor performance is obtained when $\gamma_{\text{S-CHD}}$ is low regardless the SNR of CHDs-DCD links. The figure also confirms the superiority of MLE-

TABLE III
THE ELEMENTS OF $\mathbf{F}_{l,\acute{l}}$.

$\mathbf{F}_{3l-2,3\acute{l}-2} = \frac{1}{2\pi}\sum_{i=1}^{C}\sum_{k=1}^{K_c}\beta(\boldsymbol{\theta}_l)\beta(\boldsymbol{\theta}_{\acute{l}})(x_k - x_l)(x_k - x_{\acute{l}})\mathcal{I}_{i,k}^{\text{est}}$	$\mathbf{F}_{3l-2,3\acute{l}-1} = \frac{1}{2\pi}\sum_{i=1}^{C}\sum_{k=1}^{K_c}\beta(\boldsymbol{\theta}_l)\beta(\boldsymbol{\theta}_{\acute{l}})(x_k - x_l)(y_k - y_{\acute{l}})\mathcal{I}_{i,k}^{\text{est}}$
$\mathbf{F}_{3l-2,3\acute{l}} = \frac{1}{2\pi}\sum_{i=1}^{C}\sum_{k=1}^{K_c}\beta(\boldsymbol{\theta}_l)\beta(\boldsymbol{\theta}_{\acute{l}})(x_k - x_l)(z_k - z_{\acute{l}})\mathcal{I}_{i,k}^{\text{est}}$	
$\mathbf{F}_{3l-1,3\acute{l}-2} = \frac{1}{2\pi}\sum_{i=1}^{C}\sum_{k=1}^{K_c}\beta(\boldsymbol{\theta}_l)\beta(\boldsymbol{\theta}_{\acute{l}})(y_k - y_l)(x_k - x_{\acute{l}})\mathcal{I}_{i,k}^{\text{est}}$	$\mathbf{F}_{3l-1,3\acute{l}-1} = \frac{1}{2\pi}\sum_{i=1}^{C}\sum_{k=1}^{K_c}\beta(\boldsymbol{\theta}_l)\beta(\boldsymbol{\theta}_{\acute{l}})(y_k - y_l)(y_k - y_{\acute{l}})\mathcal{I}_{i,k}^{\text{est}}$
$\mathbf{F}_{3l-1,3\acute{l}} = \frac{1}{2\pi}\sum_{i=1}^{C}\sum_{k=1}^{K_c}\beta(\boldsymbol{\theta}_l)\beta(\boldsymbol{\theta}_{\acute{l}})(y_k - y_l)(z_k - z_{\acute{l}})\mathcal{I}_{i,k}^{\text{est}}$	
$\mathbf{F}_{3l,3\acute{l}-2} = \frac{1}{2\pi}\sum_{i=1}^{C}\sum_{k=1}^{K_c}\beta(\boldsymbol{\theta}_l)\beta(\boldsymbol{\theta}_{\acute{l}})(z_k - z_l)(x_k - x_{\acute{l}})\mathcal{I}_{i,k}^{\text{est}}$	$\mathbf{F}_{3l,3\acute{l}-1} = \frac{1}{2\pi}\sum_{i=1}^{C}\sum_{k=1}^{K_c}\beta(\boldsymbol{\theta}_l)\beta(\boldsymbol{\theta}_{\acute{l}})(z_k - z_l)(y_k - y_{\acute{l}})\mathcal{I}_{i,k}^{\text{est}}$
$\mathbf{F}_{3l,3\acute{l}} = \frac{1}{2\pi}\sum_{i=1}^{C}\sum_{k=1}^{K_c}\beta(\boldsymbol{\theta}_l)\beta(\boldsymbol{\theta}_{\acute{l}})(z_k - z_l)(z_k - z_{\acute{l}})\mathcal{I}_{i,k}^{\text{est}}$	

TABLE IV
THE SIMULATION PARAMETERS USED TO OBTAIN RESULTS.

$\mathcal{K}$	σ_w^2	$\tilde{m}$	c	G_T	G_R	f (RF)	ϱ (RF)	ϱ (UW)	f (UW)	T	κ (RF,UW)
10 dB	5×10^{-8} W/Hz	1.9	3×10^{8} m/s	0 dB	0 dB	1 GHz	0	1	100 kHz	100	2

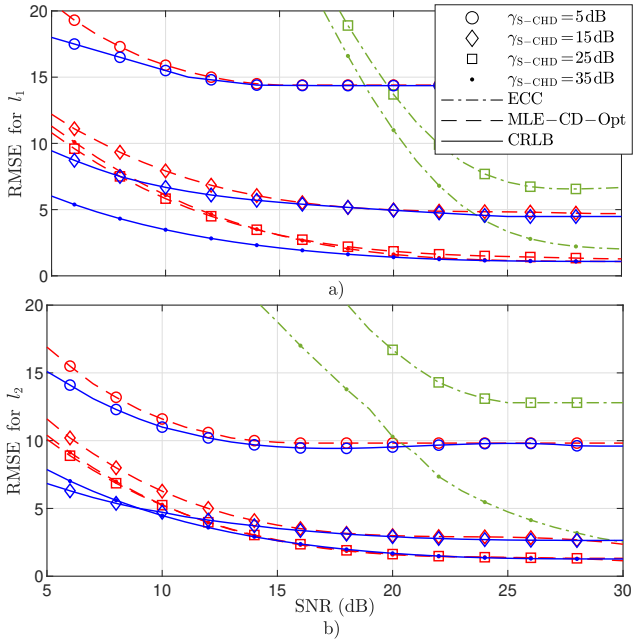

Fig. 6. The achievable RMSE for MLE-CD-Opt under different SNRs for Sensors-CHDs channels, where $K = 225$ and $M = 8$.

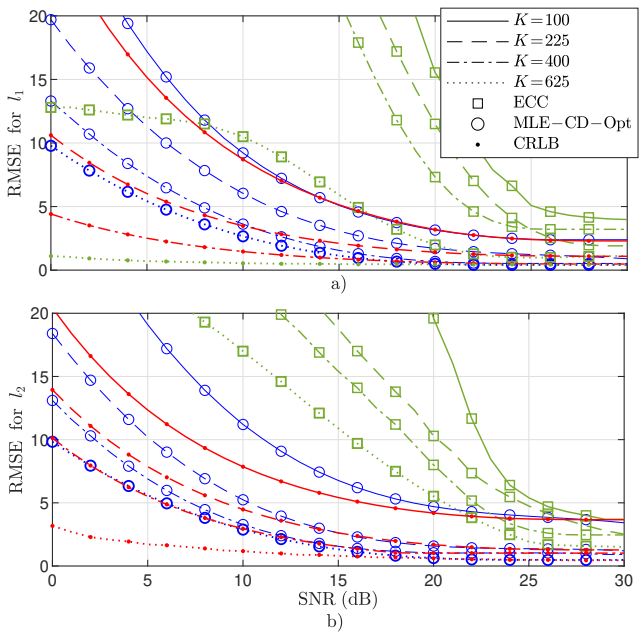

Fig. 7. The achievable RMSE for MLE-CD-Opt for different values of number of sensors K, where $\gamma_{\text{S-CHD}} = 35$ dB and $M = 8$.

CD-Opt over the used ECC benchmark, for example, RMSE obtained by using ECC is 33.5 m and 25 m for l_1 and l_2, respectively, at $\gamma_{\text{S-CHD}} = 5$ dB. It can also be seen that the deviation between the RMSE of MLE-CD-Opt and CRLB decreases as SNR increases, and converges to the same RMSE at high SNR.

Fig. 7 presents the impact of increasing the number of deployed sensors K on the achievable RMSE of MLE-CD-Opt estimator. The values of M and $\gamma_{\text{S-CHD}}$ are fixed at 8 and 35 dB, respectively. As can be observed from the figure, the localization methods can benefit from increasing K. For example, Fig. 7.a shows that at SNR $= 15$ dB, the RMSE of ECC has decreased from more than 20 m to approximately 5.5 m by increasing K from 100 to 625, while it has decreased to 12 m in Fig. 7.b under similar operating conditions. At the same value of SNR, the RMSE of MLE-CD-Opt has decreased from 5.13 m to 1.14 m in Fig. 7.a when K increases from 100 to 625, and from 6.77 m to 1.32 m in Fig. 7.b under similar assumptions. Although ECC has gained higher RMSE improvement by increasing K, it still suffers from a considerable RMSE when compared to the proposed MLE-CD-Opt. Interestingly, a significant reduction in the RMSE of MLE-CD-Opt can be achieved by increasing K and SNR, for example, an RMSE of less than 0.45 m and 0.6 m can be achieved when estimating the locations of the targets l_1 and l_2, respectively, when SNR ≥ 20 dB and $K = 625$.

Figs. 8 and 9 compare the location estimation approaches introduced in this paper in RF signalling in terrestrial environment and acoustic transmissions in underwater environments, respectively, where RMSE is plotted against the SNR of CHDs-DCD link. The values of K and M are fixed for both kinds of environments at 225 and 8, respectively. Moreover, $\gamma_{\text{S-CHD}}$ is fixed at 35 dB for the terrestrial environment, which under similar system conditions equals 40 dB for the underwater environment. As can be observed from these two figures, the optimal MLE with CD, i.e., MLE-CD-Opt, provides the best performance, whereas noncoherent ED with DTE results in poor RMSE. It can be also seen that for a

This article has been accepted for publication in IEEE Internet of Things Journal. This is the author's version which has not been fully edited and content may change prior to final publication. Citation information: DOI 10.1109/JIOT.2023.3347171

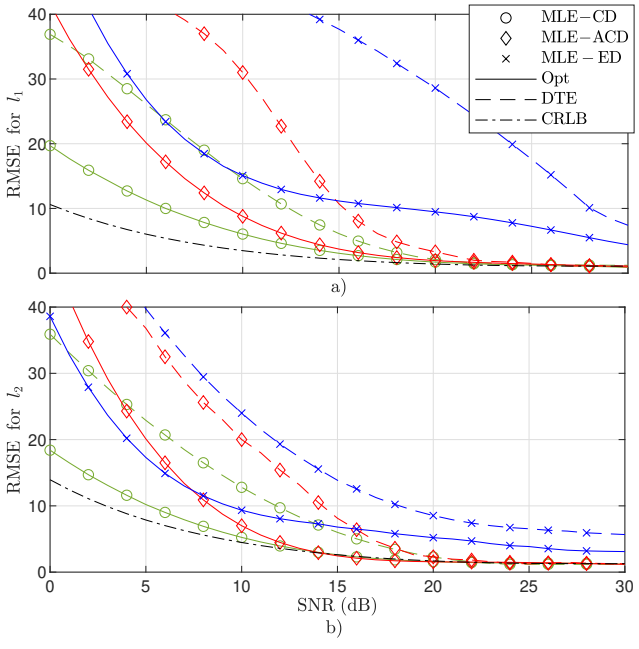

Fig. 8. A comparison between the RMSE of the introduced estimators in terrestrial environment, where $K = 225$, $M = 8$ and $\gamma_{\mathrm{S-CHD}} = 35$ dB.

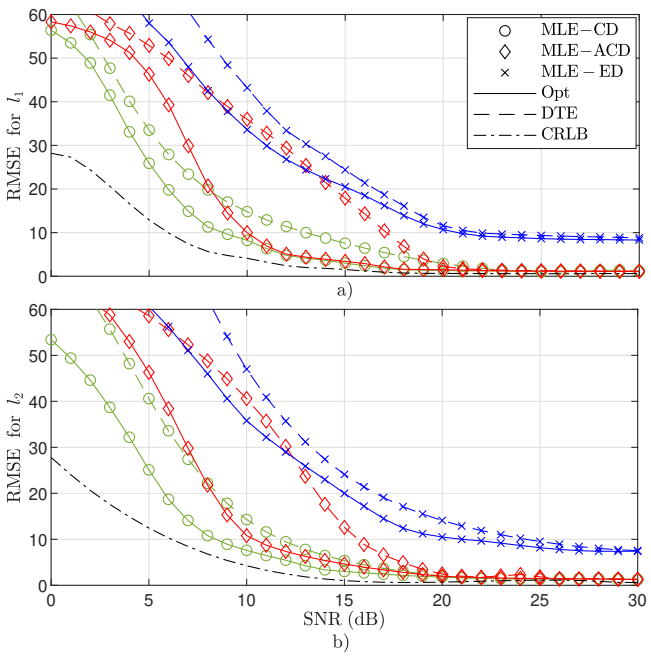

Fig. 9. A comparison between the RMSE of the introduced estimators in underwater environment, where $K = 225$, $M = 8$ and $\gamma_{\mathrm{S-CHD}} = 40$ dB.

certain detection scheme, e.g. CD, ACD or ED, the performance of the optimal MLE and DTE converges at high SNR. For example at SNR $= 20$ dB, an RMSE of about 1.6 m is obtained in Fig. 8.b, for the cases of MLE-CD-Opt and MLE-CD-DTE, while the RMSE in underwater environment reaches 1.9 m for target l_2 at the same value of SNR as shown in Fig. 9.b. This kind of convergence can be attributed to the fact that the detection stage of DTE can detect transmitted symbols with very small SER at high SNR. Interestingly, the figures also show a comparable RMSE for ACD based estimator with MLE-CD at high SNR and they both converge to the derived CRLB, although ACD provides a slightly higher SER for the whole SNR range, which has been proven in Fig. 4. Anyway, since both provide low SER at high SNR, even though CD is better, the impact of SER on RMSE is not noticeable in Figs. 8 and 9 while the RMSE becomes dominated by other system parameters such as K and M, as shown in previous figures.

Fig. 10 shows the RMSE in estimating the locations of targets located in 3D environments with $l_1 \sim (-50, 23, 5)$ m and $l_2 \sim (90, -135, 10)$ m using 2D-WSN, where the number of quantization levels is fixed at $M = 16$ and SNR from the nearest sensor to its CHD is set to $\gamma_{\mathrm{S-CHD}} = 35$ dB. Figs. 10.a and 10.b show the RMSE in xy direction (e.g. excluding the error in z direction) for targets l_1 and l_2, respectively, whereas Figs. 10.c and 10.d display the RMSE in xyz direction. It can be seen from Figs. 10.c and 10.d that 2D-WSN is capable for localizing targets located in xyz space, however, at the expense of accuracy when compared to Figs. 10.c and 10.d. For example, the RMSE for localizing l_1 is about 1.7 m in xy plane at SNR $= 30$ dB, whereas it reaches 4.8 m when z direction is included in Fig. 10.c. Moreover, the performance gap can be significantly decreased by increasing K, for example, the RMSE in the estimated location of l_2 at

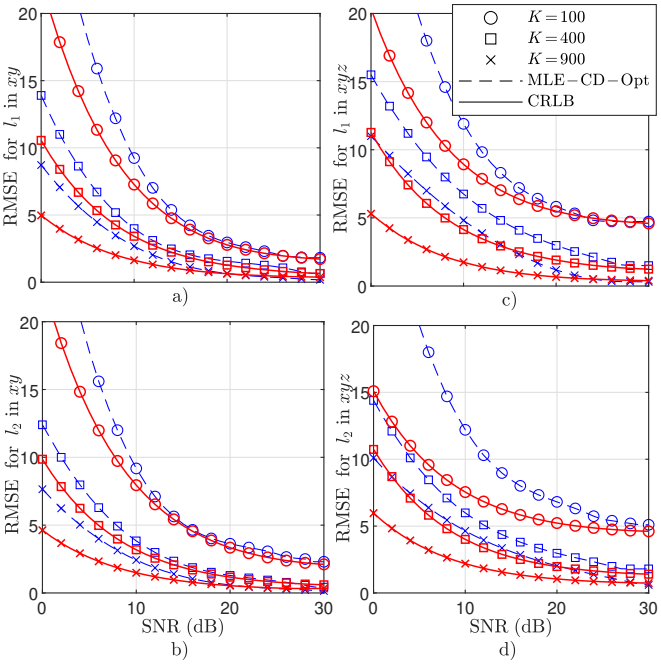

Fig. 10. The RMSE in localizing targets located in 3D space using 2D-WSN, where $M = 16$, $\gamma_{\mathrm{S-CHD}} = 35$ dB, $l_1 \sim (-50, 23, 5)$ and $l_2 \sim (90, -135, 10)$.

SNR $= 30$ dB has decreased from 5 m to 0.7 m by increasing K from 100 to 900.

Fig. 11 shows 3D plots for the log-likelihood function $\mathcal{L}_{\mathrm{CD,opt}}(\boldsymbol{\theta})$ derived in (21). For the results in this figure, a number of $K = 1600$ sensors are deployed in the environment, the number of quantization levels is $M = 16$, SNR $= 40$ dB for CHD-DCD links, and $\gamma_{\mathrm{S-CHD}} = 35$ dB for Sensors-CHD links. The value of $\tilde{m}$ is set to $\tilde{m} = 2$ in Figs. 11.a,

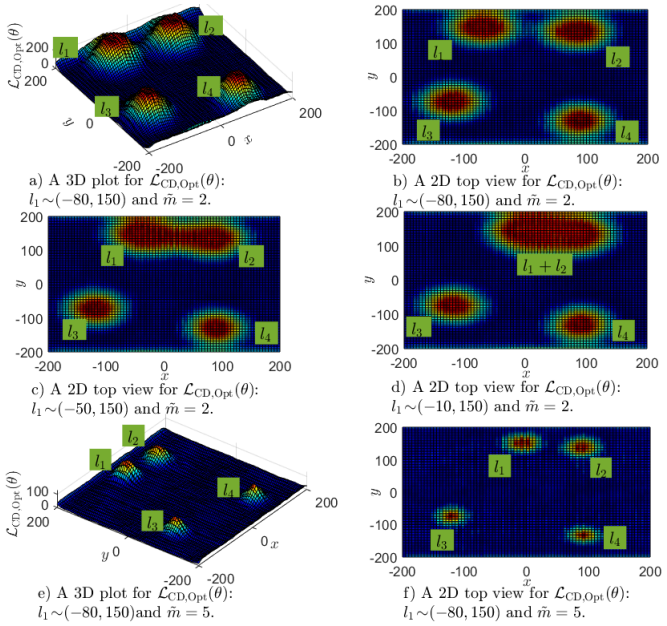

Fig. 11. 3D plots for the log-likelihood function different locations of one of the targets.

11.b, 11.c and 11.d, whereas $\tilde{m} = 5$ is used in Figs. 11.e and 11.f. All other system parameters are set according to the general theme introduced in the first paragraph of this section and Table IV. Moreover, four targets are placed in the 2D environment with fixed locations for targets $\{l_2, l_3, l_4\} \sim \{(90, 135), (-125, -77), (90, -135)\}$ whereas the location of the first target is considered dynamic as displayed in the subfigures captions. As can be observed from the figure, $\mathcal{L}_{\mathrm{CD,opt}}(\boldsymbol{\theta})$ generally has a number of bell-shaped peaks equal to the number of existing targets in the environment, which can be clearly seen in Figs. 11.a and 11.b when all targets are widely separated with $l_1 \sim (-80, 150)$. On the other hand, when l_1 moves to $(-50, 150)$ and becomes closer to l_2, as in Fig. 11.c, their peaks start to overlap with some degree, even though it can be seen that the two peaks are still separable. However, as shown in Fig. 11.d when the location of l_1 is $(-50, 150)$, the targets l_1 and l_2 become very close, and the two peaks merge into one super peak. Thus, in the latter case, the classifier, or PMLE, may not be able to distinguish between these two targets and thus it counts 3 targets rather than 4 targets, which misleads the localization process. To solve this problem, the decision thresholds used by the sensors are redesigned by increasing $\tilde{m}$ to 5, which limits the spread of target power over distance. As a result, the width of the peaks becomes smaller which makes all peaks to be distinguished again, as shown in Figs. 11.e and 11.f. It is worth noting that this approach requires deploying a large number of sensors, otherwise, that could result in ruining the system if the number of sensors is not adequate. For example, if $\tilde{m}$ increases to 10, there is a high probability that RSS at sensors falls below the least threshold level.

Table V shows the percentage of estimated number of targets $\hat{L}$ at different SNR values for CHDs-DCD link, where the actual number of potential targets in the environment is 3. To obtain the results in this table, 225 sensors are uniformly deployed in a 2D environment, the modulation order is $M = 8$, the SNR of Sensors-CHDs link is 35 dB, and the targets are located at $\{l_1, l_2, l_3\} \sim \{(-50, 23), (90, -135), (120, 80)\}$, while all other system parameters follow the description in the first paragraph of this section and Table IV. As can be noticed from the table, the accuracy of estimating the number of targets using the information criteria of interest increases as SNR improves. For example, the accuracy at 5 dB for {BIC,AIC,cAIC,HQIC} is respectively $\{99, 99, 99, 99\}\%$, whereas it reaches $\{100, 100, 100, 100\}\%$ when SNR increases to 30 dB.

Fig. 12.a and Fig. 12.b present the obtained estimates of targets positions using $T = 20$ and $T = 100$, respectively, where the empirical model in [71] has been employed to generate the RSS values measured by the sensors. The empirical model in [71] is introduced based on experimental measurements of RSS in response to a single target, however, the RSS values due to multiple targets can be generated according to the superposition principle that is well-established in physics as described in Sec. III. The simulation environment follows the LoS environment that is described in [71, Table II]. After the generation of RSS values, the processing methods carried out at the sensors and DCD are applied as described in our article. For the results in this figure, the number of quantization levels is $M = 16$, SNR $= 20$ dB for CHD-DCD links, $\gamma_{\mathrm{S-CHD}} = 20$ dB for Sensors-CHD links, and $\tilde{m} = 3$. As can be observed from the figure, the BIC based PMLE manages to separate the targets by successfully classifying all data points related to the targets. By comparing Fig. 12.a and Fig. 12.b, it can be also seen that increasing T is able enhance the localization accuracy. For example, the estimated positions are more concentrated around the actual location of the two targets in Fig. 12.a.

IX. Conclusion

In this paper we focused on estimating the number and locations of potential targets using clustered WSN in terrestrial and underwater environments. M-ASK was employed at the sensors to send their quantized decisions to the DCD with the assistance of the CHDs using the DFR protocol. At the DCD, the PMLE was applied to achieve the desired objectives, where a penalty term that depends on the number of targets L was added to the logarithmic likelihood function to enable the estimation of L. At the receiving end of the communication link, three types of detectors were considered, namely CD, ACD and NCED, which rely on whether CSI is fully or partially known. In addition, different estimators were introduced based on the availability of CSI at the DCD, and a two-stage DTE suboptimal estimator was derived that managed to provide comparable performance at high SNR. Furthermore, the CRLB was derived to serve as a benchmark for the asymptotic behavior of the proposed estimators, in addition to the ECC benchmark.

The obtained results showed that PMLE can effectively estimate the number and locations of targets when they are sufficiently separated. Furthermore, it was observed that the

TABLE V
THE ACCURACY OF ESTIMATING THE NUMBER OF TARGETS AT DIFFERENT SNRS USING DIFFERENT INFORMATION CRITERIA, WHERE THE ACTUAL NUMBER OF TARGETS IS 3.

	$\hat{L}=1$	$\hat{L}=2$	$\hat{L}=3$	$\hat{L}=4$	$\hat{L}\geq 5$
SNR (dB)	{BIC,AIC,cAIC,HQIC}%	{BIC,AIC,cAIC,HQIC}%	{BIC,AIC,cAIC,HQIC}%	{BIC,AIC,cAIC,HQIC}%	{BIC,AIC,cAIC,HQIC}%
5	{0,0,0, 0}%	{1,0, 0,0}%	{99,99,99,99}%	{0,1,1,1}%	{0,0,0, 0}%
10	{0,0,0,0}%	{0,0,0,0}%	{100,99.5,99.5,100}%	{0,0.5,0.5,0}%	{0, 0,0,0}%
20	{0,0, 0,0}%	{0, 0,0,0}%	{100,100,100,100}%	{0,0,0, 0}%	{0,0,0,0}%
30	{0,0,0,0}%	{0,0,0,0}%	{100,100,100,100}%	{0,0,0,0}%	{0,0,0, 0}%

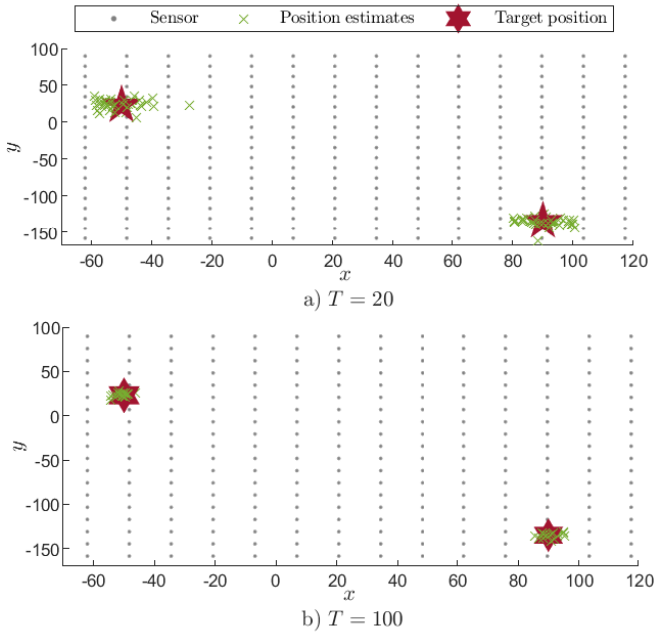

Fig. 12. Estimates of locations for two targets using BIC-PMLE, where $M = 16$, $l_1 \sim (-50, 23)$ and $l_2 \sim (90, -135)$.

RMSE is highly dependent on the total number of distributed sensors K and SNR. Moreover, it was noticed that the estimation process might be misleading when some of the targets are close in distance, however, increasing SNR and the number of sensors, as well as carefully designing the quantization thresholds at the sensors, managed to solve this issue. Furthermore, it was shown that there is a trade-off between the number of quantization levels M and the transmission link SNR, where low values of M could provide better RMSE at low SNR since large M could suffer considerable SER at low SNR. However, a higher M is generally preferable in the mid and high ranges of SNR since the RMSE in this range is dominated by M as SER is very low for all values of M.

In future, more comprehensive practical experiments will be demonstrated on large network scale to prove the applicability of the introduced system and localization algorithms. Future work would also consider a more generalized system model in which integrated localization and data communication are involved, and multi-antenna network devices are deployed. In addition, other challenges such as the impact of the targets' mobility, water waves, and harsh environmental conditions on the localization process can be taken into account. Moreover, the derivation and demonstration of the PMLE based on different types of sensory measurements such as AoA, ToA, TDoA and range estimates are interesting research topics at future.

APPENDIX I: THE DERIVATION OF PSER AND SCDP FOR CD

By substituting $\tilde{y}_{i,k}$ given in (11) in the definition of $z_{i,k}$ just below (14), we obtain $z_{i,k} = u_{i,k}^{(m)} + \frac{\mathrm{Re}\left(\tilde{h}_{i,k}^{*}\tilde{\varphi}_{i,k}\right)}{\sqrt{P_{\mathrm{s}}\mathcal{B}_i^k\left(\tilde{d}_i^k,\tilde{f}_{i,k}\right)}\left|\tilde{h}_{i,k}\right|^2}$, and thus the distribution of $z_{i,k}$ conditioned on $\tilde{h}_{i,k}$ and $u_{i,k}^{(m)}$ can be found as $z_{i,k} \sim \mathcal{N}\left(u_{i,k}^{(m)}, \frac{2\sigma_{\tilde{\varphi}}^2}{P_{\mathrm{s}}\mathcal{B}_i^k\left(\tilde{d}_i^k,\tilde{f}_{i,k}\right)\left|\tilde{h}_{i,k}\right|^2}\right)$. Therefore, the probability of deciding $\hat{u}_{i,k,\mathrm{CD}} = u_{i,k}^{(\dot{m})}$ at the receiver, i.e., CHD, conditioned on $\tilde{h}_{i,k}$ and given that $u_{i,k}^{(m)}$ has been transmitted by sensor (i,k), can be formulated as

$$\Pr\left(\hat{u}_{i,k,\mathrm{CD}} = u_{i,k}^{(\dot{m})} | u_{i,k}^{(m)}, h_{i,k}\right) = \frac{\sqrt{P_{\mathrm{s}}\mathcal{B}_i^k\left(\tilde{d}_i^k,\tilde{f}_{i,k}\right)}\left|\tilde{h}_{i,k}\right|}{\sqrt{2\pi\sigma_{\tilde{\varphi}}^2}} \times \int_{\tau_{\mathrm{CD},\dot{m}-1}}^{\tau_{\mathrm{CD},\dot{m}}} \exp\left(-\frac{P_{\mathrm{s}}\mathcal{B}_i^k\left(\tilde{d}_i^k,\tilde{f}_{i,k}\right)\left|\tilde{h}_{i,k}\right|^2}{2}\left(\frac{z_{i,k}-u_{i,k}^{(m)}}{\sigma_{\tilde{\varphi}}}\right)^2\right) dz_{i,k}. \quad (45)$$

It is worth mentioning that this probability represents PSER when $\hat{u}_{i,k,\mathrm{CD}} \neq u_{i,k}^{(m)}$, whereas it represents SCDP when $\hat{u}_{i,k,\mathrm{CD}} = u_{i,k}^{(m)}$. By substituting $\tilde{z}_{i,k} = \sqrt{P_{\mathrm{s}}\mathcal{B}_i^k\left(\tilde{d}_i^k,\tilde{f}_{i,k}\right)}\left|\tilde{h}_{i,k}\right|\frac{z_{i,k}-u_{i,k}^{(m)}}{\sigma_{\tilde{\varphi}}}$ in (45), we obtain

$$\Pr\left(\hat{u}_{i,k,\mathrm{CD}} = u_{i,k}^{(\dot{m})} | u_{i,k}^{(m)}, \tilde{h}_{i,k}\right) = \frac{1}{\sqrt{2\pi}} \int_{\tilde{\tau}_{\mathrm{CD},\dot{m}-1}}^{\tilde{\tau}_{\mathrm{CD},\dot{m}}} \exp\left(-\frac{1}{2}\tilde{z}_{i,k}^2\right) d\tilde{z}_{i,k}$$
$$= Q\left(\gamma\left(\tau_{\mathrm{CD},\dot{m}-1} - u_{i,k}^{(m)}\right)\right) - Q\left(\gamma\left(\tau_{\mathrm{CD},\dot{m}} - u_{i,k}^{(m)}\right)\right) \quad (46)$$

where $\tilde{\tau}_{\mathrm{CD},\dot{m}} = \frac{1}{\sigma_{\tilde{\varphi}}}\sqrt{P_{\mathrm{s}}\mathcal{B}_i^k\left(\tilde{d}_i^k,\tilde{f}_{i,k}\right)}|\tilde{h}_{i,k}|\left(\tau_{\mathrm{CD},\dot{m}} - u_{i,k}^{(m)}\right)$ and $\gamma = \frac{1}{\sigma_{\tilde{\varphi}}}\sqrt{P_{\mathrm{s}}\mathcal{B}_i^k\left(\tilde{d}_i^k,\tilde{f}_{i,k}\right)}\left|\tilde{h}_{i,k}\right|$. Thereafter, by evaluating the average of $\Pr\left(\hat{u}_{i,k,\mathrm{CD}} = u_{i,k}^{(\dot{m})} | u_{i,k}^{(m)}, h_{i,k}\right)$ taken over the distribution of $\tilde{\alpha} = \left|\tilde{h}_{i,k}\right|$, which is the Rician PDF, $\Pr\left(\hat{u}_{i,k,\mathrm{CD}} = u_{i,k}^{(\dot{m})} | u_{i,k}^{(m)}\right)$ can be expressed as

$$\Pr\left(\hat{u}_{i,k,\mathrm{CD}}{=}u_{i,k}^{(\dot{m})}|u_{i,k}^{(m)}\right)=\int_0^{\infty}\Pr\left(\hat{u}_{i,k,\mathrm{CD}}=u_{i,k}^{(\dot{m})}|u_{i,k}^{(m)},\tilde{\alpha}\right)f(\tilde{\alpha})d\tilde{\alpha}$$

$$=\int_0^{\infty}\left(Q\left(\tilde{\gamma}\left(\tau_{\mathrm{CD},\dot{m}-1}-u_{i,k}^{(m)}\right)\tilde{\alpha}\right)-Q\left(\tilde{\gamma}\left(\tau_{\mathrm{CD},\dot{m}}-u_{i,k}^{(m)}\right)\tilde{\alpha}\right)\right)$$
$$\times\frac{2(1+\mathcal{K})}{\Omega}\tilde{\alpha}\,\mathrm{e}^{-\mathcal{K}}\mathrm{e}^{-\mathcal{K}_A\tilde{\alpha}^2}I_0\left(2\tilde{\alpha}\sqrt{\mathcal{K}_B}\right)d\tilde{\alpha} \quad (47)$$

where $\tilde{\gamma}\triangleq\frac{\gamma}{|\tilde{h}_{i,k}|}=\frac{1}{\sigma_{\tilde{\varphi}}}\sqrt{P_{\mathrm{s}}\mathcal{B}_i^k\left(\tilde{d}_i^k,\tilde{f}_{i,k}\right)}$, $\frac{(1+\mathcal{K})}{\Omega}\triangleq\mathcal{K}_A$ and $\frac{\mathcal{K}(1+\mathcal{K})}{\Omega}\triangleq\mathcal{K}_B$. By using the tight series approximation for the Q-function introduced in [59], we obtain (48) as given on page 18, which by using [60, Eq. 2.15.5.4, pp. 306], can be found as

$$\Pr\left(\hat{u}_{i,k,\mathrm{CD}}=u_{i,k}^{(\dot{m})}|u_{i,k}^{(m)}\right)=\mathrm{e}^{-\mathcal{K}}$$
$$\times\sum_{n=1}^{n_{\max}}\epsilon_n\left(\frac{\exp\left(\frac{c^2}{4p_{\dot{m}-1,n}}\right)}{p_{\dot{m}-1,n}}-\frac{\exp\left(\frac{c^2}{4p_{\dot{m},n}}\right)}{p_{\dot{m},n}}\right) \quad (49)$$

where $p_{\dot{m},n}{=}\varepsilon_n\tilde{\gamma}^2\left(\tau_{\mathrm{CD},\dot{m}}-u_{i,k}^{(m)}\right)^2+\mathcal{K}_A$ and $c=2\sqrt{\mathcal{K}_B}$.

Appendix II:: The derivation of PSER and SCDP for NCED

By referring to (17), when $u_{i,k}^{(m)}\in\{1,2,\cdots,M-1\}$, PSER and SCDP can be written as

$$\Pr\left(\hat{u}_{i,k}^{(\dot{m})}|u_{i,k}^{(m)}\right)=\Pr\left(\gamma_{\dot{m}}\le r_{i,k}\le\gamma_{\dot{m}+1}|u_{i,k}^{(m)}\right) \quad (50)$$

where $\dot{m}\in\{0,1,2,\ldots,M-1\}$. By using the CDF of Chi-squared distribution, $\Pr\left(\hat{u}_{i,k}^{(\dot{m})}|u_{i,k}^{(m)}\right)$ can be evaluated as (51) on page 18, where $\lambda_{i,k}^{(m)}=\mu_{\tilde{r}|u_{i,k}^{(m)}}=\sqrt{P_{\mathrm{s}}\mathcal{B}_i^k\left(\tilde{d}_i^k,\tilde{f}_{i,k}\right)}\left(u_{i,k}^{(m)}\right)^2\mu_{\tilde{h}}^2$ and $\sigma_{\tilde{y}_{i,k}}^{(m)}=\sqrt{P_{\mathrm{s}}\mathcal{B}_i^k\left(\tilde{d}_i^k,\tilde{f}_{i,k}\right)\sigma_{\tilde{h}}^2\left(u_{i,k}^{(m)}\right)^2+\sigma_{\tilde{\varphi}}^2}$. On the other hand, to evaluate the remaining probabilities associated with $u_{i,k}^{(m)}=0$, the CDF of a Chi-squared random variable with 2 degrees of freedom, i.e., exponential distribution with a rate parameter of $\frac{1}{2\sigma_{\tilde{\varphi}}^2}$, is invoked [56, Eq. 2.3-24]. Consequently, PSER and SCDP in this case can be found as

$$\Pr\left(\hat{u}_{i,k}^{(\dot{m})}|u_{i,k}^{(m)}=0\right)=\exp\left(-\frac{\tau_{\mathrm{NCED},\dot{m}}}{2\sigma_{\tilde{\varphi}}^2}\right)-\exp\left(-\frac{\tau_{\mathrm{NCED},\dot{m}+1}}{2\sigma_{\tilde{\varphi}}^2}\right). \quad (52)$$

Appendix III: The derivations of $f(\breve{y}_{i,k}|\hat{u}_{i,k})$ and $\frac{\partial}{\partial\chi_l}f(\breve{y}_{i,k}|\boldsymbol{\theta})$ for FIM

By invoking the law of total probability, the PDF $f(\breve{y}_{i,k}|\hat{u}_{i,k})$ can be evaluated by integrating the product of $f(\breve{y}_{i,k}|\hat{u}_{i,k},\alpha_{i,k})$ and $f(\alpha_{i,k})$ over the range of $\alpha_{i,k}$, as given in (53) on page 18. Then, by using the series expansion of the modified Bessel function [66], $f(\breve{y}_{i,k}|\hat{u}_{i,k})$ can be written as (54) on page 18 which can be solved using [67, Eq. 2.3.15.3, pp. 343] as shown in (55) on page 19, where $D(\cdot)$ is the parabolic cylinder function.

The partial derivative $\frac{\partial}{\partial\chi_l}f(\breve{y}_{i,k}|\boldsymbol{\theta})$ can be evaluated as

$$\frac{\partial}{\partial\chi_l}f(\breve{y}_{i,k}|\boldsymbol{\theta})=\sum_{\hat{u}_{i,k}}\sum_{u_{i,k}}f(\breve{y}_{i,k}|\hat{u}_{i,k})\Pr(\hat{u}_{i,k}|u_{i,k})\frac{\partial}{\partial\chi_l}\Pr(u_{i,k}|\boldsymbol{\theta}) \quad (56)$$

which, after substituting the definition of $\Pr(u_{i,k}|\boldsymbol{\theta})$ given in (7) and evaluating its derivative, can be expressed as

$$\frac{\partial f(\breve{y}_{i,k}|\boldsymbol{\theta})}{\partial\chi_l}=\frac{1}{\sqrt{2\pi}}\sum_{\hat{u}_{i,k}}\sum_{u_{i,k}}f(\breve{y}_{i,k}|\hat{u}_{i,k})\Pr(\hat{u}_{i,k}|u_{i,k})\mathcal{B}_m(\boldsymbol{\theta})$$
$$\times\frac{\partial}{\partial\chi_l}\left(\frac{\mu_{s_k}(\boldsymbol{\theta})}{\sigma_{s_k}(\boldsymbol{\theta})}\right) \quad (57)$$

where

$$\mathcal{B}_m(\boldsymbol{\theta})=\exp\left(-\left(\frac{\tau_{m-1}-\mu_{s_k}(\boldsymbol{\theta})}{\sqrt{2}\sigma_{s_k}(\boldsymbol{\theta})}\right)^2\right)-\exp\left(-\left(\frac{\tau_m-\mu_{s_k}(\boldsymbol{\theta})}{\sqrt{2}\sigma_{s_k}(\boldsymbol{\theta})}\right)^2\right). \quad (58)$$

The last term in (57), $\frac{\partial}{\partial\chi_l}\left(\frac{\mu_{s_k}(\boldsymbol{\theta})}{\sigma_{s_k}(\boldsymbol{\theta})}\right)$, can be evaluated as

$$\frac{\partial}{\partial\chi_l}\left(\frac{\mu_{s_k}(\boldsymbol{\theta})}{\sigma_{s_k}(\boldsymbol{\theta})}\right)=\frac{\partial}{\partial\chi_l}\left(\frac{\sigma_w^2+\left(A_k^{\Sigma}(\boldsymbol{\theta})\right)^2}{\sqrt{\frac{2\sigma_w^4}{T}+4\frac{\sigma_w^2}{T}\left(A_k^{\Sigma}(\boldsymbol{\theta})\right)^2}}\right)$$
$$=\Psi(\boldsymbol{\theta})\times\frac{\partial}{\partial\chi_l}A_k^{\Sigma}(\boldsymbol{\theta}) \quad (59)$$

where $\Psi(\boldsymbol{\theta})$ is given by

$$\Psi(\boldsymbol{\theta})=\frac{4\sigma_w^2\sqrt{T}\left(A_k^{\Sigma}(\boldsymbol{\theta})\right)^3}{\left(2\sigma_w^4+4\sigma_w^2\left(A_k^{\Sigma}(\boldsymbol{\theta})\right)^2\right)^{\frac{3}{2}}}. \quad (60)$$

Eventually, by using the definitions of $A_k^{\Sigma}(\boldsymbol{\theta})\triangleq\sum_{l=1}^{L}A_k^l(\boldsymbol{\theta})$ and $A_k^l(\boldsymbol{\theta})=\sqrt{B_k^l\left(d_k^l,f\right)}$ along with $B_k^l\left(d_k^l,f\right)$ as defined in (1), then $\frac{\partial}{\partial\chi_l}A_k^{\Sigma}(\boldsymbol{\theta})$ can be evaluated as

$$\frac{\partial}{\partial\chi_l}A_k^{\Sigma}(\boldsymbol{\theta})=\frac{\partial}{\partial\chi_l}\left(\sum_{l=1}^{L}\sqrt{P_l}\left(\frac{d_0}{d_k^l}\right)^{0.5\kappa}a(f)^{0.5\left(d_0-d_k^l\right)^{\varrho}}\right)$$
$$=\beta(\boldsymbol{\theta}_l)(x_k-x_l) \quad (61)$$

where

$$\beta(\boldsymbol{\theta}_l)=\frac{\sqrt{P_l}d_0^{0.5\kappa}a(f)^{0.5\left(d_0-d_k^l\right)^{\varrho}}}{2\left(d_k^l\right)^{1+0.5\kappa}}$$
$$\times\left(\kappa\left(d_k^l\right)^{-1}+\varrho\left(d_0-d_k^l\right)^{\varrho-1}\ln a(f)\right). \quad (62)$$

References

[1] M. Al-Jarrah. M. Yaseen. A. Al-Dweik, O. Dobre, and E. Alsusa, "Decision fusion for IoT-based wireless sensor networks," *IEEE IoT J.*, vol. 7, no. 2, pp. 1313-1326, Feb. 2020.

[2] S. Tomic, B. Marko, R. Dinis, M. Tuba, N. Bacanin. RSS-AoA-based Target Localization and Tracking in WSNs. River Publishers: Aalborg, Denmark, 2020.

[3] S. Shiraki and S. Shioda, "Contact information-based indoor pedestrian localization using bluetooth low energy beacons," *IEEE Access*, vol. 10, pp. 119863-119874, 2022.

[4] D. Ciuonzo, G. Romano, and P. Rossi, "Channel-aware decision fusion in distributed MIMO WSNs: decode-and-fuse vs. decode-then-fuse," *IEEE Trans. Wireless Commun.*, vol. 11, no. 8, pp. 2976 – 2985, Aug. 2012.

[5] M. Al-Jarrah, N. Al-Ababneh, M. Al-Ibrahim, and R. Al-Jarrah, "Co-operative OFDM for semi-distributed detection in wireless sensor networks," *AEU-Int. J. Electron. Commun.*, vol. 68, no. 10, pp. 1022-1029, Oct. 2014.

[6] P. Zhang, I. Nevat, G. Peters, G. Xiao, and H. Tan, "Event detection in WSNs in random spatial sensors deployments," *IEEE Trans. Signal Process.*, vol. 63, no. 22, pp. 6122-6135, Jul. 2015.

$$\Pr\left(\hat{u}_{i,k,\mathrm{CD}}=u_m|u_{i,k}\right)=\frac{2}{\mathrm{e}^{\mathcal{K}}}\sum_{n=1}^{n_{\max}}\epsilon_n\left(\int_0^{\infty}\tilde{\alpha}\exp\left(-\left[\varepsilon_n\tilde{\gamma}^2\left(\tau_{\mathrm{CD},m-1}-u_{i,k}\right)^2+\mathcal{K}_A\right]\tilde{\alpha}^2\right)I_0\left(2\tilde{\alpha}\sqrt{\mathcal{K}_B}\right)d\tilde{\alpha}\right.$$
$$\left.-\int_0^{\infty}\tilde{\alpha}\exp\left(-\left[\varepsilon_n\tilde{\gamma}^2\left(\tau_{\mathrm{CD},m}-u_{i,k}\right)^2+\mathcal{K}_A\right]\tilde{\alpha}^2\right)I_0\left(2\tilde{\alpha}\sqrt{\mathcal{K}_B}\right)\right)d\tilde{\alpha}, \quad (48)$$

$$\Pr\left(\hat{u}_{i,k}^{(\dot{m})}|u_{i,k}^{(m)}\right)=\begin{cases}Q_1\left(\frac{\lambda_{i,k}^{(m)}}{\sigma_{y_{i,k}}^{(m)}},\frac{\sqrt{\tau_{\mathrm{NCED},\dot{m}+1}}}{\sigma_{y_{i,k}}^{(m)}}\right)-Q_1\left(\frac{\lambda_{i,k}^{(m)}}{\sigma_{y_{i,k}}^{(m)}},\frac{\sqrt{\tau_{\mathrm{NCED},\dot{m}}}}{\sigma_{y_{i,k}}^{(j)}}\right), & \tau_{\mathrm{NCED},\dot{m}}>\tau_{\mathrm{NCED},m}\\ 1-\left(Q_1\left(\frac{\lambda_{i,k}^{(m)}}{\sigma_{y_{i,k}}^{(m)}},\frac{\sqrt{\tau_{\mathrm{NCED},\dot{m}+1}}}{\sigma_{y_{i,k}}^{(m)}}\right)-Q_1\left(\frac{\lambda_{i,k}^{(m)}}{\sigma_{y_{i,k}}^{(m)}},\frac{\sqrt{\tau_{\mathrm{NCED},\dot{m}}}}{\sigma_{y_{i,k}}^{(m)}}\right)\right), & \tau_{\mathrm{NCED},\dot{m}}<\tau_{\mathrm{NCED},m}\end{cases} \quad (51)$$

$$f\left(\breve{y}_{i,k}|\hat{u}_{i,k}\right)=\int_0^{\infty}f\left(\breve{y}_{i,k}|\hat{u}_{i,k},\alpha_{i,k}\right)f\left(\alpha_{i,k}\right)d\alpha_{i,k}$$
$$=\frac{2\mathcal{K}_A\,\mathrm{e}^{-\mathcal{K}}}{\sqrt{2\pi\sigma_{\varphi}^2}}\int_0^{\infty}\alpha_{i,k}\,\mathrm{e}^{-\alpha_{i,k}^2}\,\mathrm{e}^{-\frac{1}{2\sigma_{\varphi}^2}\left(\breve{y}_{i,k}-\sqrt{\tilde{P}_i\mathcal{B}_i^{\mathrm{c}}\left(d_i^{\mathrm{c}},f_i^{\mathrm{c}}\right)}\alpha_{i,k}\hat{u}_{i,k}\right)^2}I_0\left(2\alpha_{i,k}\sqrt{\mathcal{K}_B}\right)d\alpha_{i,k} \quad (53)$$

$$f\left(\breve{y}_{i,k}|\hat{u}_{i,k}\right)=\frac{2\,\mathrm{e}^{-\mathcal{K}}}{\sqrt{2\pi\sigma_{\varphi}^2}}\sum_{m=0}^{\infty}\frac{\mathcal{K}_A\mathcal{K}_B^{\frac{m+1}{2}}}{\Gamma^2\left(m+1\right)}\int_0^{\infty}\alpha_{i,k}^{m+2}$$
$$\times\exp\left(-\frac{1}{2\sigma_{\varphi}^2}\left(\breve{y}_{i,k}^2-2\breve{y}_{i,k}\sqrt{\tilde{P}_i\mathcal{B}_i^{\mathrm{c}}\left(d_i^{\mathrm{c}},f_i^{\mathrm{c}}\right)}\hat{u}_{i,k}\alpha_{i,k}+\left(\tilde{P}_i\mathcal{B}_i^{\mathrm{c}}(d_i^{\mathrm{c}},f_i^{\mathrm{c}})\,\hat{u}_{i,k}^2+2\sigma_{\varphi}^2\mathcal{K}_A\right)\alpha_{i,k}^2\right)\right)d\alpha_{i,k} \quad (54)$$

[7] M. Al-Jarrah, R. Al-Jarrah, and N. Al-Ababneh "Decision fusion in mobile WSNs using cooperative multiple symbol differential space time coding," *AEU-Int. J. Electron. Commun.*, vol. 80, no. 2017, pp. 127-136, Oct. 2017.

[8] H. Shi, W. Gao, Y. Liu, B. Wang, and H. Zhao, "An adaptive multi-homogeneous sensor weight calculation method for body sensor networks," *IEEE Access*, vol. 7, pp. 121629-121644, 2019.

[9] M. Wong, Q. Lu, and S.-H. Chan, "SiFu: A generic and robust multimodal signal fusion platform for pervasive localization," *IEEE IoT J.*, vol. 10, no. 1, pp. 904-919, 2023.

[10] J. Hu, L. Xie, and C. Zhang, "Energy-based multiple target localization and pursuit in mobile sensor networks," *IEEE Trans. Instrum. Meas.*, vol. 61, no. 1, pp. 212-220, Jan. 2012.

[11] A. Vempaty, Y.S. Han, and P. Varshney, "Target localization in WSNs using error correcting codes," *IEEE Trans. Inf. Theory*, vol. 60, no. 1, pp. 697-712, Jan. 2014.

[12] D. Salinas, A. Pascoal, and J. Aranda, "Optimal sensor placement for acoustic underwater target positioning with range-only measurements," *IEEE J. Ocean. Eng.*, vol. 41, no. 3, pp. 620-643, Jan. 2016.

[13] C. Wei, P. Chen, Y. Han, and P. Varshney, "Local threshold design for target localization using error correcting codes in WSNs in the presence of Byzantine attacks," *IEEE Trans. Inf. Forensics Security*, vol. 12, no. 7, pp. 1571-1584, Jul. 2017.

[14] R. Niu, A. Vempaty, and P. Varshney, "Received-signal-strength-based localization in wireless sensor networks," *Proc. IEEE*, vol. 106, no. 7, pp. 1166–1182, Jul. 2018.

[15] Y. Li, Z. He, Y. Li, Z. Gao, R. Chen, and N. El-Sheimy, "Enhanced wireless localization based on orientation-compensation model and differential received signal strength," *IEEE Sensors J.*, vol. 19, no. 11, pp. 4201-4210, Jun. 2019.

[16] M. Al-Jarrah, A. Al-Dweik, E. Alsusa, and E. Damiani, "RFID reader localization using hard decisions with error concealment," *IEEE Sensors J.*, vol. 19, no. 17, pp. 7534-7542, Sep. 2019.

[17] M. A. Al-Jarrah, A. Al-Dweik, N. Ali, and E. Alsusa, "Joint estimation of location and orientation in wireless sensor networks using directional antennas," *IEEE Sensors J.*, vol. 20, no. 23, pp. 14347-14359, Dec. 2020.

[18] H. Qi, L. Mo, and X. Wu, "SDP relaxation methods for RSS/AOA-based localization in sensor networks," *IEEE Access*, vol. 8, pp. 55113-55124, 2020.

[19] S. Chang, Y. Zheng, P. An, J. Bao, and J. Li, "3-D RSS-AOA based target localization method in wireless sensor networks using convex relaxation," *IEEE Access*, vol. 8, pp. 106901-106909, 2020.

[20] W. Gifford, D. Dardari, and M. Win, "The impact of multipath information on time-of-arrival estimation," *IEEE Trans. Signal Process.*, vol. 70, pp. 31-46, 2022.

[21] C.-Y. Wei and C.-C. Chen, "Cube-based multitarget 3D localization using Bayesian learning-based turbo decoding in WSNs," *IEEE Sensors J.*, vol. 22, no. 17, pp. 17291-17306, 2022.

[22] W. Liu, M. Haardt, M. Greco, C. Mecklenbräuker, and P. Willett, "Twenty-five years of sensor array and multichannel signal processing: A review of progress to date and potential research directions," *IEEE Signal Process. Mag.*, vol. 40, no. 4, pp. 80-91, 2023.

[23] L. Caceres Najarro, I. Song, and K. Kim, "Fundamental limitations and state-of-the-art solutions for target node localization in WSNs: A review," *IEEE Sensors J.*, vol. 22, no. 24, pp. 23661-23682, Dec. 2022.

[24] H. Ketabalian, M. Biguesh, and A. Sheikhi, "A closed-form solution for localization based on RSS," *IEEE Trans. Aerosp. Electron. Syst.*, vol. 56, no. 2, pp. 912-923, Apr. 2020.

[25] S. Kumar and S. Das, "Target detection and localization methods using compartmental model for internet of things," *IEEE Trans. Mobile Comput.*, vol. 19, no. 9, pp. 2234-2249, Sep. 2020.

[26] A. Ababneh, "Low-complexity bit allocation for RSS target Localization," *IEEE Sensors J.*, vol. 19, no. 17, pp. 7733-7743, 2019.

[27] X. Mei, H. Wu, and J. Xian, "Matrix factorization-based target localization via range measurements with uncertainty in transmit power," *IEEE Wireless Commun. Lett.*, vol. 9, no. 10, pp. 1611-1615, 2020.

[28] H. Huang, W. Miao, G. Min, C. Huang, X. Zhang, and C. Wang, "Resilient range-based d-dimensional localization for mobile sensor networks," *IEEE/ACM Trans. Netw.*, vol. 28, no. 5, pp. 2037-2050, 2020.

[29] G. Wang, S. Marano, J. Zhu, and Z. Xu, "Target localization by unlabeled range measurements," *IEEE Trans. Signal Process.*, vol. 68, pp. 6607-6620, 2020.

[30] B. Yang, Q. Qiu, Q.-L. Han, and F. Yang, "Received signal strength indicator-based indoor localization using distributed set-membership filtering," *IEEE Trans. Cybern.*, vol. 52, no. 2, pp. 727-737, 2022.

[31] H. Zhu, H. Chen, and M. Luo, "Adaptive event-driven robust set-membership estimation for received-signal-strength-based moving targets localization," *IEEE IoT J.*, vol. 9, no. 14, pp. 12825-12835, 2022.

[32] H. Zhu, H. Wu, and M. Luo, "Environmentally adaptive event-driven robust cubature Kalman filter for RSS-based targets tracking in mobile WSN," *IEEE IoT J.*, vol. 10, no. 6, pp. 5530-5542, 2023.

$$f(\breve{y}_{i,k}|\hat{u}_{i,k}) = \frac{2\mathcal{K}_A\,\mathrm{e}^{-\mathcal{K}}}{\sqrt{2\pi\sigma_\varphi^2}} \sum_{m=0}^{\infty} \mathcal{K}_B^{\frac{m+1}{2}} \frac{\Gamma(m+3)}{\Gamma^2(m+1)} \left(\frac{1}{\sigma_\varphi^2}\left(\tilde{P}_i\mathcal{B}_i^{\mathrm{c}}\left(d_i^{\mathrm{c}}, f_i^{\mathrm{c}}\right)\hat{u}_{i,k}^2 + 2\sigma_\varphi^2\mathcal{K}_A\right)\right)^{-\frac{m+3}{2}}$$
$$\times \exp\left(\frac{\breve{y}_{i,k}^2}{2\sigma_\varphi^2}\left(\frac{\tilde{P}_i\mathcal{B}_i^{\mathrm{c}}\left(d_i^{\mathrm{c}}, f_i^{\mathrm{c}}\right)\hat{u}_{i,k}^2}{2\left(\tilde{P}_i\mathcal{B}_i^{\mathrm{c}}\left(d_i^{\mathrm{c}}, f_i^{\mathrm{c}}\right)\hat{u}_{i,k}^2 + 2\sigma_\varphi^2\mathcal{K}_A\right)} - 1\right)\right) D_{-(m+3)}\left(-\frac{\breve{y}_{i,k}\sqrt{\tilde{P}_i\mathcal{B}_i^{\mathrm{c}}\left(d_i^{\mathrm{c}}, f_i^{\mathrm{c}}\right)}\hat{u}_{i,k}}{\sigma_\varphi\sqrt{\tilde{P}_i\mathcal{B}_i^{\mathrm{c}}\left(d_i^{\mathrm{c}}, f_i^{\mathrm{c}}\right)\hat{u}_{i,k}^2 + 2\sigma_\varphi^2\mathcal{K}_A}}\right). \quad (55)$$

[33] N. Saeed, H. Nam, T. Al-Naffouri, and M.-S. Alouini, "A state-of-the-art survey on multidimensional scaling-based localization techniques," *IEEE Commun. Surveys Tuts.*, vol. 21, no. 4, pp. 3565-3583, Fourth-quarter 2019.

[34] J. Luo, Y. Yang, Z. Wang, and Y. Chen, "Localization algorithm for underwater sensor network: A review," *IEEE IoT J.*, vol. 8, no. 17, pp. 13126-13144, 2021.

[35] I. Ullah, Y. Liu, X. Su, and P. Kim, "Efficient and accurate target localization in underwater environment," *IEEE Access*, vol. 7, pp. 101415-101426, 2019.

[36] G. Qiao, C. Zhao, F. Zhou, and N. Ahmed, "Distributed localization based on signal propagation loss for underwater sensor networks," *IEEE Access*, vol. 7, pp. 112985-112995, 2019.

[37] Y. Su, L. Guo, Z. Jin, and X. Fu, "A mobile-beacon-based iterative localization mechanism in large-scale underwater acoustic sensor networks," *IEEE IoT J.*, vol. 8, no. 5, pp. 3653-3664, 2021.

[38] Y. Li, M. Liu, S. Zhang, R. Zheng, and J. Lan, "Node dynamic localization and prediction algorithm for internet of underwater things," *IEEE IoT J.*, vol. 9, no. 7, pp. 5380-5390, 2022.

[39] Y. Li, M. Liu, S. Zhang, R. Zheng, J. Lan, and S. Dong, "Particle system-based ordinary nodes localization with delay compensation in UWSNs," *IEEE Sensors J.*, vol. 22, no. 7, pp. 7157-7168, 2022.

[40] A. Weiss *et al.*, "A semi-blind method for localization of underwater acoustic sources," *IEEE Trans. Signal Process.*, vol. 70, pp. 3090-3106, 2022.

[41] J. Pelletier, B. O'Neill, J. Leonard, L. Freitag, and E. Gallimore, "AUV-assisted diver navigation," *IEEE Robot. Autom. Lett.*, vol. 7, no. 4, pp. 10208-10215, 2022.

[42] P. Qian, Y. Guo, N. Li, and Z. Xu, "Block variational Bayesian algorithm for multiple target localization with unknown and time-varying transmit powers in WSNs," *IEEE Access*, vol. 7, pp. 54796-54808, 2019.

[43] P. Qian, Y. Guo, and N. Li, "Multitarget localization with inaccurate sensor locations via variational EM algorithm," *IEEE Sensors Lett.*, vol. 3, no. 2, pp. 1-4, Feb. 2019.

[44] P. Zuo, T. Peng, K. You, W. Guo, and W. Wang, "RSS-based localization of multiple directional sources with unknown transmit powers and orientations," *IEEE Access*, vol. 7, pp. 88756-88767, 2019.

[45] K. You, W. Guo, T. Peng, Y. Liu, P. Zuo, and W. Wang, "Parametric sparse Bayesian dictionary learning for multiple sources localization with propagation parameters uncertainty," *IEEE Trans. Signal Process.*, vol. 68, pp. 4194-4209, 2020.

[46] P. Qian, Y. Guo, N. Li, and D. Fang, "Compressive sensing based multiple source localization in the presence of sensor position uncertainty and nonuniform noise," *IEEE Access*, vol. 6, pp. 36571-36583, 2018.

[47] B. Sun, Y. Guo, N. Lim and D. Fang, "An efficient counting and localization framework for off-grid targets in WSNs," *IEEE Commun. Lett.*, vol. 21, no. 4, pp. 809-812, Apr. 2017.

[48] Y. Guo, B. Sun, N. Li, and D. Fang, "Variational Bayesian inference-based counting and localization for off-grid targets with faulty prior information in wireless sensor networks," *IEEE Trans. Commun.*, vol. 66, no. 3, pp. 1273-1283, Mar. 2018.

[49] A. Stefanov and M. Stojanovic, "Design and performance analysis of underwater acoustic networks," *IEEE J. Sel. Areas Commun.*, vol. 29, no. 10, pp. 2012-2021, Dec. 2011.

[50] E. Panayirci, M. Altabbaa, M. Uysal, and H. V. Poor, "Sparse channel estimation for OFDM-based underwater acoustic systems in Rician fading with a new OMP-MAP algorithm," *IEEE Trans. Signal Process.*, vol. 67, no. 6, pp. 1550-1565, Mar. 2019.

[51] M. Al-Jarrah, K. Park, A. Al-Dweik, and M.-S. Alouini, "Error rate analysis of amplitude-coherent detection over Rician fading channels with receiver diversity," *IEEE Trans. Wireless Commun.*, vol. 19, no. 1, pp. 134-147, Jan. 2020.

[52] M. Al-Jarrah, E. Alsusa, A. Al-Dweik, and D. K. C. So, "Capacity analysis of IRS-based UAV communications with imperfect phase compensation," *IEEE Wireless Commun. Lett.*, vol. 10, no. 7, pp. 1479-1483, Jul. 2021.

[53] M. Al-Jarrah, A. Al-Dweik, E. Alsusa, Y. Iraqi, and M.-S. Alouini, "On the performance of IRS-assisted multi-layer UAV communications with imperfect phase compensation," *IEEE Trans. Commun.*, vol. 69, no. 12, pp. 8551-8568, Dec. 2021.

[54] Y. Yang, Y. Xiao, and T. Li, "A survey of autonomous underwater vehicle formation: Performance, formation control, and communication capability," *IEEE Commun. Surveys Tut.*, vol. 23, no. 2, pp. 815-841, Secondquarter 2021.

[55] T. Rappaport. *Wireless Communications: Principles and Practice,* 2nd ed. Upper Saddle River, N.J.: Prentice Hall PTR, 2002.

[56] J. Proakis and M. Salehi. *Digital Communications*. 5th ed. McGraw-Hill, New York, 2008.

[57] A. Al-Dweik and Y. Iraqi, "Error probability analysis and applications of amplitude-coherent detection in flat Rayleigh fading channels," *IEEE Trans. Commun.*, vol. 64, no. 5, pp. 2235–2244, May 2016.

[58] M. A. Al-Jarrah, A. Al-Dweik, K.-H. Park, and M.-S. Alouini, "Amplitude-coherent detection for optical wireless communications: Opportunities and limitations," *IEEE Open J. Commun. Soc.*, vol. 1, pp. 550-562, 2020.

[59] I. Tanash and T. Riihonen, "Global minimax approximations and bounds for the Gaussian Q-function by sums of exponentials," *IEEE Trans. Commun.*, vol. 68, no. 10, pp. 6514–6524, Oct. 2020.

[60] A. P. Prudnikov, Yu. A. Brychkov, and O. I. Marichev. *Integrals and Series: Special Functions*. Gordon and Breach Science Publishers, UK, 3rd edition, 1986.

[61] A. Al-Dweik, Y. Iraqi, K.-H. Park, M. Al-Jarrah, E. Alsusa, M.-S. Alouini, "Efficient NOMA design without channel phase information using amplitude-coherent detection," *IEEE Trans. Commun.*, vol.70, no.1, pp.245-263, 2022.

[62] R. Mallik and R. Murch, "Optimal ASK levels for channel magnitude based diversity reception in Rayleigh fading," *IEEE Trans. Commun.*, vol. 66, no. 9, pp. 4345-4360, Sep. 2018.

[63] A. Agarwal, C. Psomas, and I. Krikidis, "Communication systems with amplitude detection: An asymptotic approach," *IEEE IoT J.*, vol. 9, no. 19, pp. 18319-18332, Oct., 2022.

[64] A. Mariani, A. Giorgetti and M. Chiani, "Model order selection based on information theoretic criteria: Design of the penalty," *IEEE Trans. Signal Process.*, vol. 63, no. 11, pp. 2779-2789, Jun., 2015.

[65] H. Poor. *An introduction to signal detection and estimation*, 2nd ed. New York: Springer-Verlag, 1994.

[66] M. Abramowitz and I. Stegun. *Handbook of Mathematical Functions with Formulas*, New York, 1972.

[67] A. P. Prudnikov, Yu. A. Brychkov, and O. I. Marichev. *Integrals and Series: Elementary Functions*. Gordon and Breach Science Publishers, UK, 3rd edition, 1986.

[68] N. Bulusu, J. Heidemann, and D. Estrin, "GPS-less low-cost outdoor localization for very small devices," *IEEE Pers. Commun.*, vol. 7, no. 5, pp. 28-34, Oct. 2000.

[69] K. Magowe, A. Giorgetti, S. Kandeepan, and X. Yu, "Accurate analysis of weighted centroid localization," *IEEE Trans. Cogn. Commun. Netw.*, vol. 5, no. 1, pp. 153-164, Mar. 2019.

[70] K. Magowe, A. Giorgetti, and K. Sithamparanathan, "Closed-form approximation of weighted centroid localization performance," *IEEE Sensors Lett.*, vol. 3, no. 12, pp. 1-4, Dec. 2019, Art no. 7501304.

[71] R. Sandoval, A.-J. Garcia-Sanchez, and J. Garcia-Haro, "Improving RSSI-based path-Loss models accuracy for critical infrastructures: A smart grid substation case-study," *IEEE Trans. Ind. Informat.*, vol. 14, no. 5, pp. 2230-2240, May 2018.

BIOGRAPHIES

Mohammad Al-Jarrah (Member, IEEE) received the B.Sc. and M.Sc. degrees in electrical engineering/wireless communications from Jordan University of Science and Technology (JUST), Irbid, Jordan, in 2008 and 2011, respectively. He received his Ph.D. degree in electrical and electronics engineering from The University of Manchester, Manchester, U.K in 2023.

He had been working as a lecturer at Prince Sattam Bin Abdulaziz University (PSAU), Al-Riyadh, Saudi Arabia from 2011 to 2017, and as a Lab Instructor with Khalifa University (KU), Abu Dhabi, United Arab Emirates (UAE) from 2017 to 2019. Currently, he is working with the Department of Electrical and Electronic Engineering, The University of Manchester, as a Post-Doctoral Research Associate (PDRA).

Dr. Al-Jarrah is a recipient of the Jordanian Royal Scholarship and Marie Skłodowska-Curie Actions (MSCA) fellowship from the European Union (EU). His research interests include diverse topics in wireless communications and signal processing: distributed decision fusion systems, statistical signal processing, localization and tracking, RFID communications, spectrum sensing, integrated radar-communications, intelligent reflecting surfaces (IRSs), and backhauling and cellular planning for future communication networks.

Emad Alsusa (M'06–SM'07) is the head of the Communication and RF Research Group at the Department of Electrical and Electronic Engineering at the University of Manchester. His research interest is in the area of Wireless Networks and Signal Processing with particular focus on future ultra-efficient networks through the design of novel techniques for radio resource management, interference manipulation, joint sensing and communications, novel waveforms, and physical layer security. Emad is a senior member of the Institute of Electrical and Electronic Engineers (IEEE, USA) and a UK representative in the International Union of Radio Science (URSI). He served as a conference general co/Chair of the IEEE OnlineGreencom in 2017 and Sustainability through ICT Summit in 2019, as well as a TPC Symposia-co/Chair in several IEEE conferences including VTC'16, GISN'16, PIMRC'17, Globecom'18 and Globecomm'23. He is an Editor of the IEEE Wireless Communications Letters and the IEEE Transactions on Vehicular Technology. Emad has received a number of awards including the best paper awards in the IEEE international Symposium on Power Line Communications in 2014, the IEEE Wireless Communications and Networking Conference in 2019, and in the IEEE International Symposium on Networks, Computers and Communications (ISNCC'21).

Arafat Al-Dweik (Senior Member, IEEE) received the M.S. (Summa Cum Laude) and Ph.D. (Magna Cum Laude) degrees in electrical engineering from Cleveland State University, Cleveland, OH, USA, in 1998 and 2001, respectively.

He is currently with the Department of Electrical Engineering and Computer Science, Khalifa University, Abu Dhabi, UAE. He also worked at Efficient Channel Coding, Inc., Cleveland, OH, USA, Department of Information Technology, Arab American University, Jenin, Palestine, and University of Guelph, ON, Canada. He is a Visiting Research Fellow with the School of Electrical, Electronic, and Computer Engineering, Newcastle University, Newcastle upon Tyne, U.K, and a Research Professor with Western University, London, ON, Canada, and University of Guelph, Guelph, Canada. He has extensive research experience in various areas of wireless communications that include modulation techniques, channel modeling and characterization, synchronization and channel estimation techniques, OFDM technology, error detection and correction techniques, MIMO, and resource allocation for wireless networks.

Prof. Al-Dweik serves as an Associate Editor for the IEEE Transactions on Vehicular Technology and the IET Communications. He is a member of Tau Beta Pi and Eta Kappa Nu. He was awarded the Fulbright scholarship from 1997 to 1999. He was the recipient of the Hijjawi Award for Applied Sciences in 2003, Fulbright Alumni Development Grant in 2003 and 2005, Dubai Award for Sustainable Transportation in 2016, UAE Leader-Founder Award in 2019. He is a Registered Professional Engineer in the Province of Ontario, Canada.